2-D CFD Design of the Cross-Sectional Shape of Arterial Stents

By

Kristen Catherine Karman

Approved:

W. Kyle Anderson
Professor of Computational Engineering
(Committee Member)

Stephen Nichols
Research Associate Professor of Computational Engineering
(Committee Member)

Robert Melnik
Research Professor of Computational Engineering
(Committee Member)

2-D CFD Design of the Cross-Sectional Shape of Arterial Stents

By

Kristen Catherine Karman

A Thesis Submitted to the Faculty of the University
of Tennessee at Chattanooga in Partial
Fulfillment of the Requirements of the
Degree of Master of Science
in Engineering

The University of Tennessee, Chattanooga
Chattanooga, Tennessee

December 2013

ABSTRACT

An approach for desigining arterial stents to maximize wall shear stress is presented. A cost equation to maximize wall shear stress is derived and then inverted into a minimization problem for the optimizer. A 2-D mixed-element finite-volume scheme for solving the compressible Navier-Stokes equations is implemented. A paramaterization of the cross-sectional shape of the stent wire using Hicks-Henne functions is described. The strategies used in the commercial optimization software, DAKOTA, to minimize the cost equation are described. The solver is validated using well known fluid flow test cases and is shown to match other published computed results for bloodflow through stented arteries. New candidate stent shapes are produced by the optimization and are evaluated based on comparison to modern commercial stent designs.

DEDICATION

This is dedicated to my parents, Deb and Steve, and my sisters, Danielle and Melissa.

Without your constant support and encouragement, none of this would have been possible.

ACKNOWLEDGEMENTS

I would like to thank Dr. Steve Karman and Dr. Robert Melnik for helping me pursue my interest in biology and biological engineering and for your patience and support throughout this endeavor. Further thanks go to Dr. W. Kyle Anderson and Dr. Stephen Nichols for their assistance in helping me to understand the various components of this research. Finally, I would like to thank Dr. Timothy Swafford and everyone else at the SimCenter for giving me the opportunity to study here and creating a helpful and encouraging environment.

TABLE OF CONTENTS

CHAPTER

LIST OF TABLES

LIST OF FIGURES

LIST OF MEDICAL TERMINOLOGY

atherosclerosis - The condition in which fat, cholesterol, and other substances builds up on the arterial walls to form plaques which can eventually block the artery and cause other problems throughout the circulatory system.

percutaneous coronary intervention (PCI) - Also known as coronary angioplasty or angioplasty is a non-surgical procedure used to treat stenotic (narrowed) arteries. A deflated angioplasty balloon is inserted into the artery and inflated where the blockage is, removing the plaque and restoring blood flow through the artery. The damage to the arterial wall from the plaque and the inflation of the balloon often necessitate the use of an stent.

stent - A cylindrical, mesh-like, metal or plastic tube which is inserted into a damaged blood vessel to help maintain the structure of the vessel walls.

stenosis - A narrowing of the of the opening of a blood vessel.

restenosis - The condition in which plaque reforms in a blood vessel that has been treated for atherosclerosis.

in-stent restenosis - The condition in which plaque build up on top of the stent after treatment for atherosclerosis.

intima - The inner lining of a blood vessel. It is made up of the endothelium, the subendothelial layer, and an elastic layer.

endothelium - The thin layer of cells which lines the interior of blood vessels. These cells are called endothelial cells.

endothelialization - The formation of endothelial tissue. When this process is complete, the injurt to the blood vessel is considered to have been healed.

(neointimal) hyperplasia - The thickening of the intima of a blood vessel as a response to injury.

elastic recoil - In relation to blood vessels, elastic recoil is the tendency of the blood vessel wall to revert to the deformed shape after injury.

smooth muscle cells - The cellular components of the blood vessel wall responsible for providing structural integrity. In response to injury, the smooth muscle cells (SMCs) also synthesize extracellular matrix molecules, migrate, and proliferate.

extracellular matrix - Molecules which help maintain the structure of the vessel wall. They aid in the formation of scar tissue, but in excess can lead to fibrosis.

fibrosis - The reparative or reactive response to injury resulting in the formation of connective tissue. This refers both to normal scarring and also the pathological depositing of excess connective tissue.

thrombosis - The formation of a thrombus (otherwise known as a blood clot) within a blood vessel which obstructs the flow of blood.

systole - The contraction of the heart, during which time blood is forced into the aorta and pulmonary artery.

diastole - The dilatation of the heart after systole in which the chambers of the heart fill with blood.

hematocrit - The volume percentage of red blood cells in blood.

erythrocytes - The red blood cells.

CHAPTER 1

INTRODUCTION

Atherosclerosis is the major cardiovascular cause of death in the Western world and is a major cause of heart attack and stroke [1]. It is characterized by the accumulation of lipids on the inner layer (intima) of arteries causing inflammation, fibrosis, and hyperplasia of the endothelium [1, 2]. Atherosclerosis can alter the flow of blood downstream by creating a stenosis (a narrowing of the arterial opening), by causing the formation of a thrombus (a blood clot) which is carried downstream to a narrower part of the artery and forms a blockage there, and by damaging the structural integrity of the vessel wall [1]. Although this process can occur anywhere throughout the body, this build up of cellular material most often occurs at bends and branches in the arterial tree [2]. Atherosclerosis does not usually occur in areas that have high wall shear stress (WSS), but instead prefers areas that have low average shear stress, secondary flows, or variable shear stress over a cardiac cycle [1].

Percutaneous coronary intervention (PCI) has become the most widely used treatment for atherosclerosis since its introduction in the late 1970s [3]. PCI involves removing the blockage by dilating the artery with an angioplasty balloon. Bare metal stents (BMS), cylindrical mesh-like structures, were developed as an adjunct to PCI for management of early complications [3]. Although the stents had success in reducing elastic recoil [3], 30-40% of patients experienced in-stent restenosis (ISR), the condition in which scar tissue (caused by intimal proliferation) builds and reforms the blockage on top of the stents [3]. Drug-eluting stents (DES) were developed as a solution for ISR and initially showed to be very effective at reducing ISR [3, 4]. However DES slow the re-endothelialization of the blood vessel and clinical studies and autopsy findings indicate that although DES may decrease early ISR, they inherently increase the risk of late stent thrombosis (LST) and delayed restenosis [3, 4].

Jukema *et al.* sought to identify the risk factors which contribute to restenosis [5]. They identified the inflammatory response to the endothelial injury from the balloon dilation and the stent placement as playing a key role. Many of the risk factors they cite are either patient-related (genetic risk factors, the presence of other arterial diseases, or hypersensitivity to some component of the stent) or lesion-related (due to the length or complexity of the lesion). Most research in stent design has been focused on material strength, biocompatibility, flexibility, drug coatings, and improved methods of deployment [6]. However, it has also been shown that the affect of the strut geometry on the local hemodynamics is such that it creates an atherosclerosis prone environment, increasing the chances of restenosis and thrombosis [4, 6]. Thus, it would be advantageous to create a stent design which minimizes the stent's affect on local hemodynamics.

The Effect of Geometry on Wall Shear Stress and Blood Flow

Any type of obstacle, whether it be blockage from atherosclerotic plaque or the presence of a stent, affects the hemodynamics of the blood vessel. Figures 1.1 and 1.2 use the abbreviation ESS. This stands for endothelial shear stress and is synonymous with wall shear stress. As illustrated in 1.1B, restenosis disturbs flow in BMS and DES treated arteries in a similar way as the initial plaque buildup in an atherosclerotic artery [4]. In either case, there is a region of high WSS and accelerated flow as the blood travels over the obstacle and then the flow separates from the wall, creating a recirculation zone and a region of low WSS, as can be seen in Figure 1.1A.

These regions of low and high WSS created by the obstacle affect the particles suspended in blood in different ways. Although high WSS is typically beneficial in the prevention of atherosclerosis and restenosis, if the shear rates are too high, it can activate platelets to

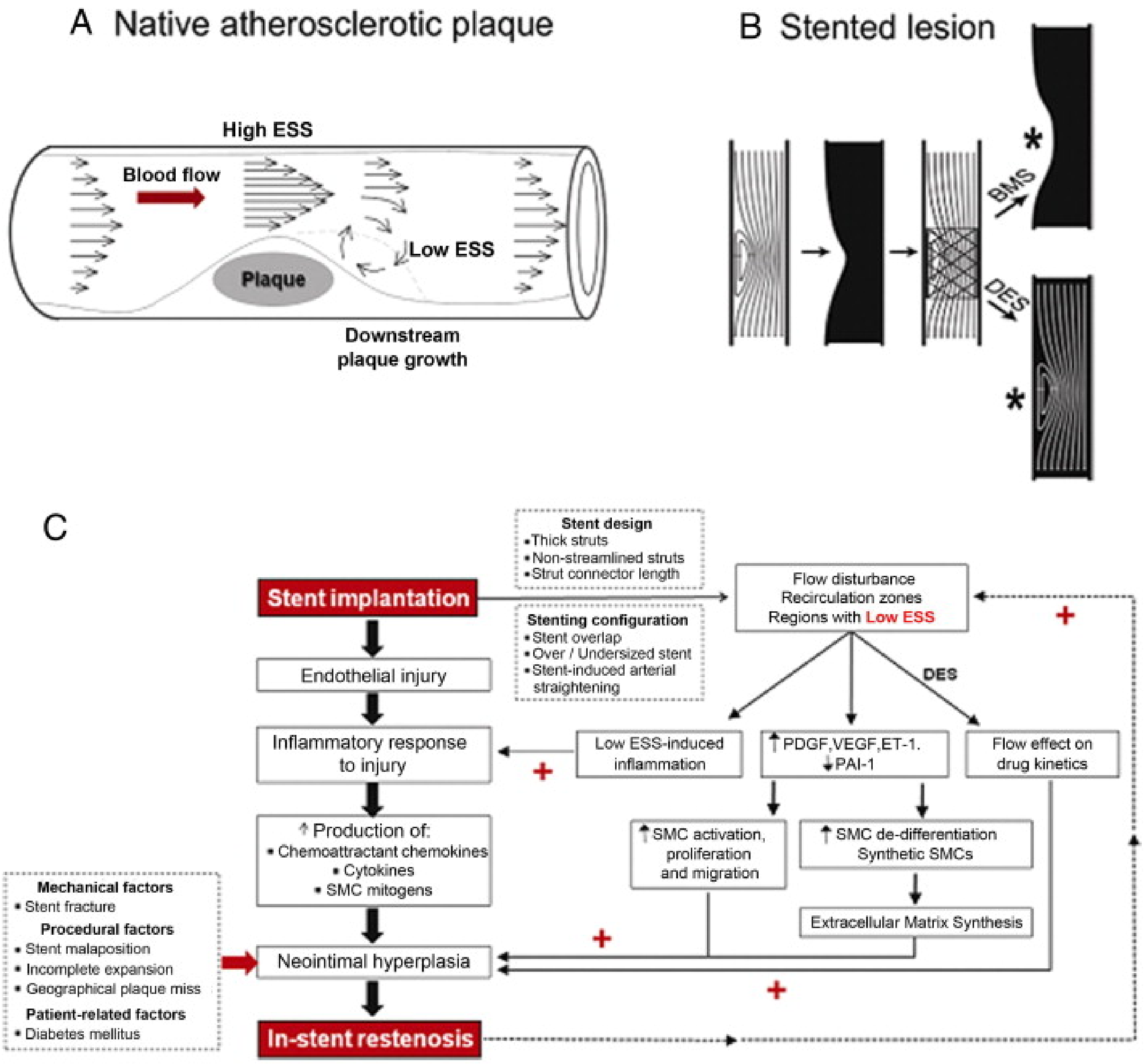

Figure 1.1 Role of Wall Shear Stress in In-Stent Restenosis
[4]

release thromboxane A_2 (TXA_2) and adenosine diphoshate (ADP), both of which promote platelet aggregation [6], [4]. These particles pass over the obstacle and become entraped in the recirculation zone. The low WSS in the recirculation zone suppresses the production of nitric oxide (NO) and endothelial prostacyclin (PGI_2), which are both platelet inhibitors

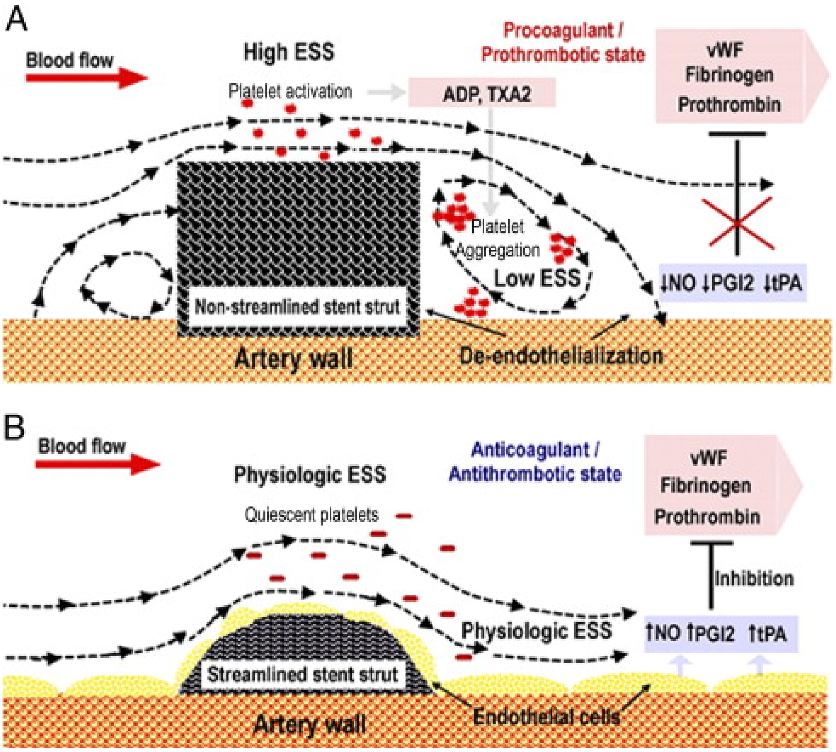

Figure 1.2 The Effect of Strut Geometry on Stent Thrombogenicity [4]

and anti-coagulants, and tissue plasminogen activator (tPA), a thrombolytic agent. It also increases production of the coagulation factor von Willebrand Factor (vWF) [6] and inhibits endothelial cell proliferation, which would normally produce an anti-coagulant phenotype [4]. Altogether, this creates an environment which favors platelet aggregation and thrombogenesis. Figure 1.2A illustrates this process in relation to flow over a rectangular stent strut [4].

Additionally, low WSS up-regulates proinflammatory genes (adhesion molecules, chemoattractant chemokines, and cytokines) which enhances the inflammation response caused by the injury to the blood vessel [4]. Low WSS also increases production of molecules which activate smooth muscle cell (SMC) proliferation and migration while it decreases production of molecules that inhibit this process (including NO and PGI_2). Furthermore, low WSS also causes these SMCs to shift into synthetic mode and produce more extracellular matrix molecules [4]. The SMCs and the extracellular matrix molecules are the principal elements in neointimal hyperplasia (NIH), which is principally responsible for ISR [6]. These contributions of WSS to ISR are summarized in Figure 1.1C.

Most currently available commercial stents use a rectangular cross-sectional shape. As can be seen in Figure 1.2A this configuration causes two recirculation zones, a small recirculation zone at the front of the stent and a larger recirculation zone at the back of the stent. Jimenez and Davies found that decreasing the width of rectangular cross-sectional strut decreases the size of the recirculation zone and the area of the endothelium exposed to recirculation, increasing the probability of endothelialization [6]. Alternatively, the design of the stent could also be improved by using a more streamlined cross-sectional shape. As illustrated in Figure 1.2B, the streamlined shape can reduce or even eliminate flow separation and bring the regions of low WSS and high WSS closer to physiological levels in the vicinity of the struts [6].

Measurements of WSS

As with many parts of the body, accurate measurements of WSS and shear rate in living people is difficult to obtain. Katritsis *et al.* examined the various means currently available for measuring wall shear stress and shear rate in blood vessels and their results are summarized in this section. Methods of these measurements fall into 3 categories: in vitro measurements, in vivo measurements, and computational approximations. In vitro methods obtain measurements using models of the circulatory system [2]. These models are often transparent glass tubes with side branches or casts of actual vessels and the methods for obtaining measurements include flow visualization using dye injection, laser Doppler anamometry, and particle image velocimetry [7]. Although these methods are useful in helping to understand the properties of the fluid itself, they do little to help visualize the conditions within the body.

In vivo methods obtain measurements directly or indirectly, invasively or non-invasively in living organisms. Invasive methods use probes placed inside the blood vessel to obtain measurements of various aspects of the blood flow. These methods all disturb the natural flow conditions within the vessel and thus actual values of WSS may be different than the values obtained by these methods [7]. Some examples of invasive techniques include:

- *Intravascular Doppler Ultrasound.* This method measures flow velocities using intravascular Doppler wires. A major disadvantage of this technique is that it can only measure the peak value of velocity and cannot provide information at the wall [7]. If Poiseuille flow is assumed, then the Hagen-Poiseuille formula can be used with this value of velocity and the diameter of the vessel to obtain an estimate of the WSS.

- *Intravascular Ultrasound.* In this method, velocity profiles are measured based on the decorrelation of ultrasonic radio-frequency signals using miniaturized transducer assemblies inserted into catheters [7]. The shear rate is obtained from the velocity profile and multiplied by the viscosity to obtain the WSS. The disadvantages to this method are that it assumes blood to be Newtonian and it cannot be used in the coronary arteries because there are no probes available that have adequate resolution to measure velocities there.

Noninvasive methods do not have the inherent flaw which is present in invasive methods. However, they are often limited by the resolution of the available technology. Noninvasive methods include:

- *Ultrasound.* This technique can determine the mean wall shear rate at the anterior and posterior vessel wall, the time-averaged and peak wall shear rate over one cardiac cycle, the value at peak systole, and the maximum change in wall shear rate within the cardiac cycle [7]. However, the nearest a value can be obtained to the wall is only 250 to 300 μm, wall shear rates can only be reliably determined in relatively straight vessels, and it cannot be applied to coronary arteries because of overlying bone and tissue.

- *Pulsed Doppler Ultrasound.* This technique measures average velocities in a target volume of a focused acoustic wave [7]. However, the smallest the target volume can be reduced to is 1 mm^3 which does not give an adequate resolution of the velocity profile. Furthermore, this technique cannot differentiate between the slowly moving vessel wall and slowly moving blood flowing near the vessel wall. As with the intravascular Doppler ultrasound, assuming Poiseuille flow, the WSS can be approximated using the velocity in the center of the vessel and the diameter of the vessel. This method also cannot be applied to coronary arteries due to the overlying bone and tissue.

- *Phase Contrast MRI.* Magnetic resonance imaging is capable of examining almost any vessel in the body, even if there is overlying bone or tissue [7]. Its limitations lie in the pixelation of the image. A given pixel may be covered partially by moving blood and partially by the stationary wall, making it difficult to precisely identify the boundary between the wall and the flow of blood. The spatial resolution is only 0.5-1.0mm, so measurements of shear rates and shear stress are not precise.

Many of the above in vitro and in vivo methods arrive at estimations for WSS and shear rate by assuming Poiseuille flow. However, Poiseuille flow makes several assumptions about the fluid and the nature of the flow [7]:

1. Blood behaves like a Newtonian fluid.

2. The flow is laminar and fully developed. This is valid in most parts of circulation, but flow can become turbulent in the largest blood vessels or at sites of pathologic deformations of arterial structure where streamlines may not be parallel to the wall.

3. Blood does not slip at the vessel wall. This is held to be universally true for all fluids (including blood).

4. The flow is steady. In reality, blood flow is pulsatile.

5. The vessel is cylindrical. Most arteries have approximately circular cross-section, but many veins and the pulmonary arteries tend to be elliptical. Also, the requirement of constant diameter is never met because individual arteries tend to become narrower as they progress toward the periphery (veins behave in the reverse way).

6. The vessel wall is rigid. Blood vessels are distensible and their diameter changes with transmural pressure.

Blood is considered a non-Newtonian fluid because it shows two kinds of shear-dependent properties: 1) the apparent viscosity increases at low shear rates; and 2) in small vessels, the apparent viscosity is smaller (at higher shear rates) than it is in larger vessels [1]. The viscosity of blood is actually dependent on the hematocrit (Hct., a percentage representing the concentration of erythrocytes), the shear rate, the size of the blood vessel, and blood temperature [7]. Figure 1.3 shows the viscosity of blood as a function of shear rate for different Hct [1]. Although the viscosity of blood varies greatly for low shear rates, it is essentially constant for shear rates $> 100s^{-1}$. Therefore, the assumption that blood is a Newtonian fluid is valid in medium and large arteries only for rates of shear $> 100s^{-1}$ [7].

The final method of obtaining measurements of WSS and shear rate is through computational fluid dynamics (CFD) simulations. According to Katritsis *et al.*, the limitations of CFD when applied to blood flow come from defining the problem, rather than from the accuracy of the numerical model [7]. Many of the assumptions made concerning Poiseuille flow are also made in CFD simulations to simplify the problem. Comparison of results obtained from steady-state Newtonian and non-Newtonian models revealed that the distribution pattern of WSS is similar, but that the magnitude of the estimate depends on

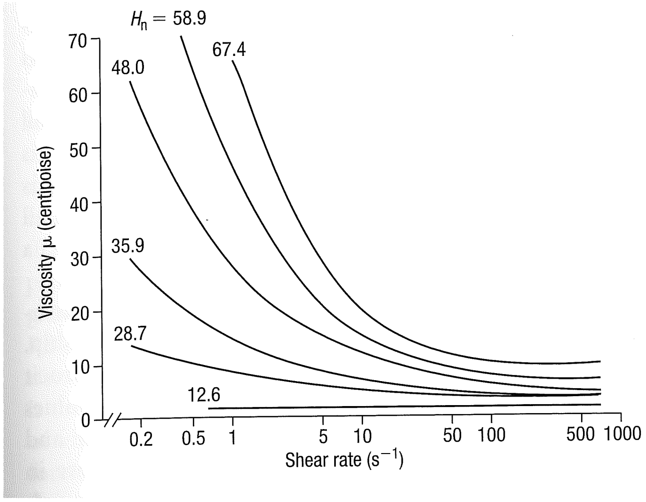

Figure 1.3 Blood Viscosity for Different Hct.
[1]

the model used [7]. Furthermore, in comparing the Newtonian and non-Newtonian models for pulsatile flow, it was observed that the Newtonian models yielded lower WSS values throughout the entire cardiac cycle, but that the distribution pattern of WSS was again similar. Thus the Newtonian assumption is an adequate approximation of the distribution pattern for WSS, but not necessarily for the magnitude. The most important limitation, however, is that there is no accepted standard against which any of these methods can be verified and that all methods of WSS measurement produce at best only approximations to the actual WSS values.

CHAPTER 2

APPROACH

The goal of this study is to use numerical methods to solve the compressible Navier-Stokes equations and determine values for WSS and shear rate and to then use a commercially available optimization software to find a design which will maximize shear rate (and thus WSS) in the vicinity of the stent. The components required to accomplish this are an optimization problem which can be phrased as a minimization problem and the optimizer. The optimizer requires a way to change the mesh according to new design variables (the mesh movement routine) and a way to evaluate the cost function (the flow solver). The optimization software chosen for this study was Dakota and it further requires that the mesh movement and the flow solver be linked together by a driver script, which it calls whenever it requires a function evaluation.

Optimization

Dakota (Design Analysis Kit for Optimization and Terascale Applications) contains algorithms to solve minimization problems using gradient or non-gradient based methods [8]. In addition to specifying the optimization method, design variables, tolerances, etc., the user also needs to provide Dakota with a means of obtaining evaluations of the cost function (and, if applicable, the derivatives of the cost function). This is typically done through a script which translates requests from Dakota into input for the program evaluating the cost (such as a flow solver) and then translates the output from this program back into the format Dakota requires. A simplified outline of this process is provided in Figure 2.1.

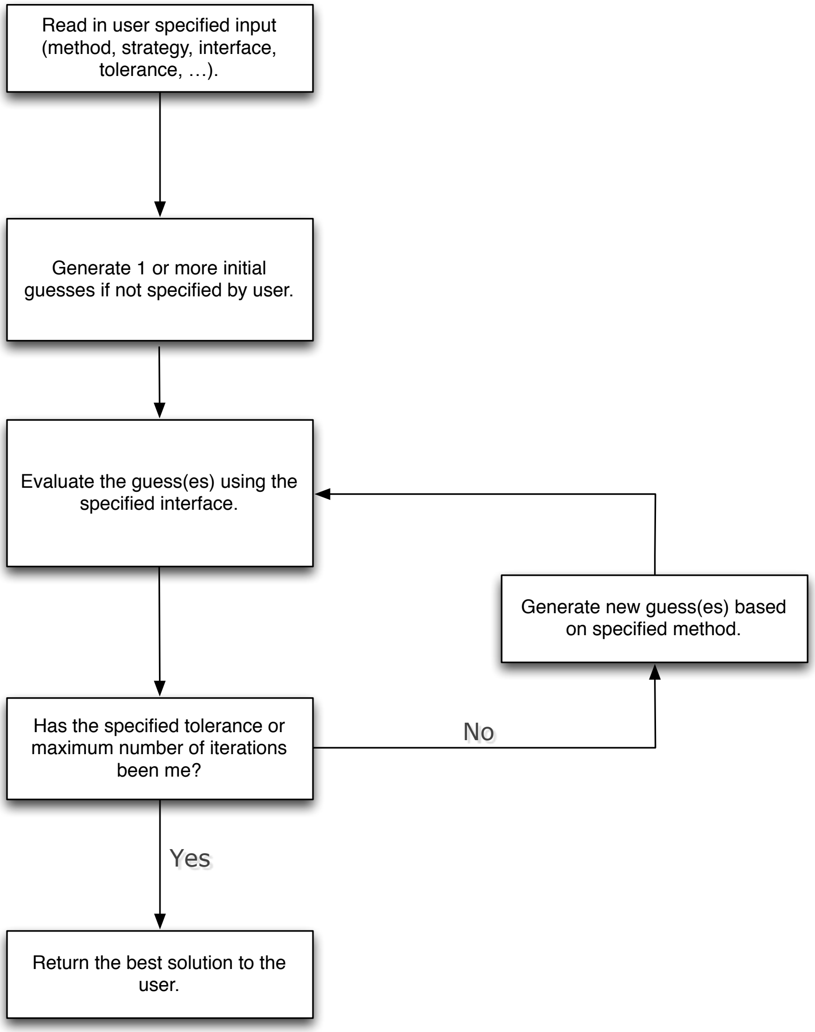

Figure 2.1 Illustration of Dakota's Optimization Process

A python script was used in this study to interface between Dakota and the flow solver. In this implementation, the design variables were the coefficients of the basis functions used to parametrize the shape of the stent (this is explained later in this chapter). In this case the application of the design variables involves moving the boundary of the mesh to a new location and smoothing the interior points. After the mesh is moved, the script makes a system call to the flow solver and then translates the output into a format that Dakota can understand. Figure 2.2 illustriates the actions performed by the driving script. Also, note that the driving script is the "specified interface" mentioned in Figure 2.1. For an example of the Dakota input file used in this study, refer to appendix A.

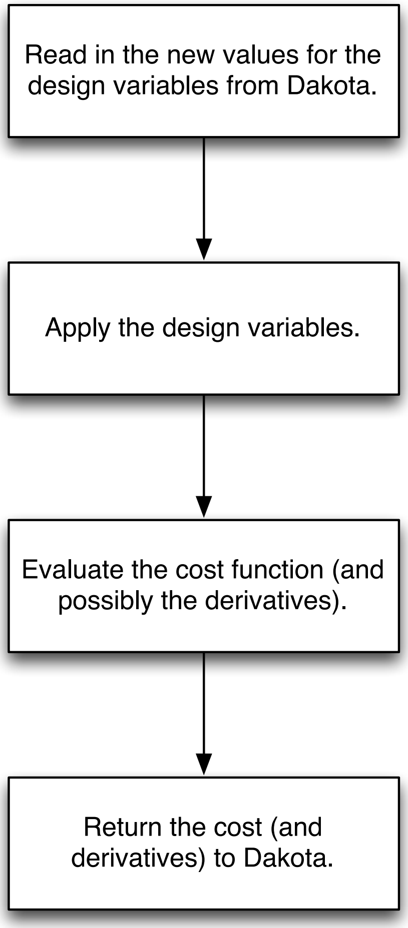

Figure 2.2 Illustration of the Steps Performed by the Driver Script

Evolutionary Algorithms

Dakota's evolutionary algorithm, coliny_ea, was the chosen method for optimization in this study. Evolutionary algorithms (EAs) are global optimization methods which are suitable for solving problems that have multiple local optima and problems in which gradients are not available or are expensive to compute [9]. These methods are based on Darwin's theory of survival of the fittest and the process is illustrated in Figure 2.3. The EA treats design points as members of a population and the design parameters as DNA. The algorithm starts with a randomly selected population of design points within the parameter space. Through a sequence of generations, members of the population are ranked based on their objective function evaluation (with low objective function values being considered the most "fit") and only the fittest are allowed to survive and reproduce [9]. The EA simulates evolution through mathematical analogs of natural selection, breeding, and mutation, ultimately identifying a design point (or a family of design points) that minimize the objective function [9].

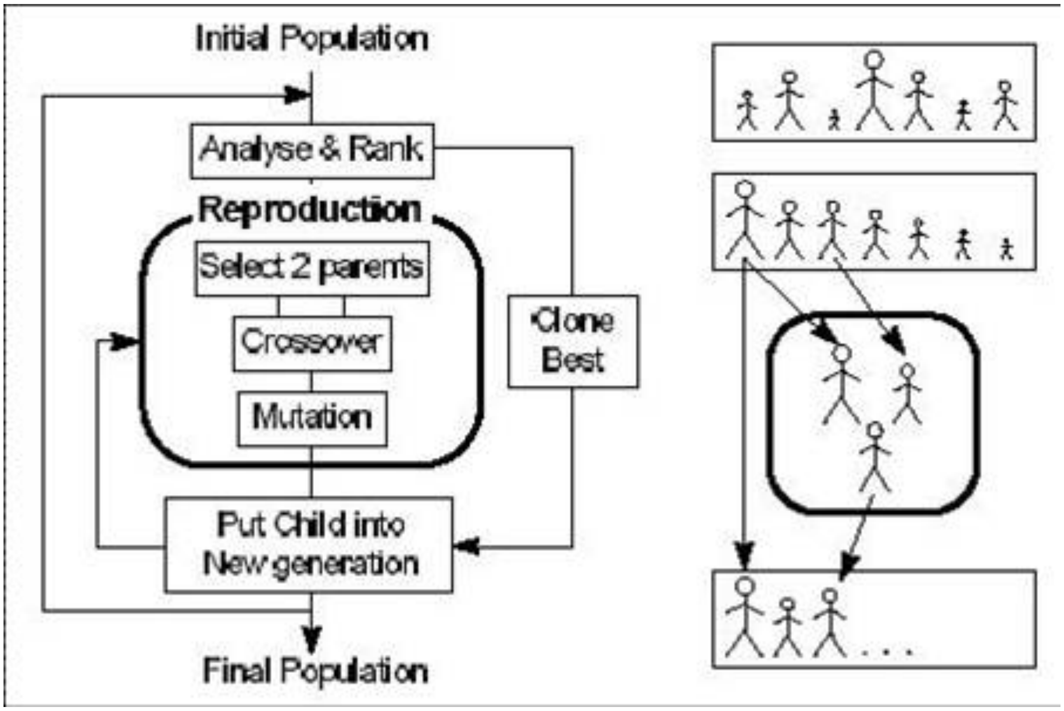

Figure 2.3 Illustration of the Evolutionary Algorithm
[8]

Cost Function

It has been shown that low shear rates are a contributing factor to the development of restenosis and that blood behaves like a Newtonian fluid for shear rates > 100. Thus a design is sought which not only maximizes the wall shear rate but also ensures that the value everywhere along the wall is > 100. However, DAKOTA is set up to solve minimization problems, so this maximization problem needs to be reprhased as a minimization problem. Equation 2.1 shows the proposed cost function for minimization based on shear rate.

$$Cost = \sum \frac{1}{(S^*)^2} \tag{2.1}$$

where the summation is over all points on the wall within an appropriate region of the stent and S^* is the local non-dimensional shear rate. Dimensional shear rate is given by

$$\begin{aligned}
S &= 2\sqrt{S_{12}^2 + \frac{1}{2}\left(S_{11}^2 + S_{22}^2\right)} && (2.2)\\
S_{12} &= \frac{1}{2}\left(\frac{\partial u}{\partial y} + \frac{\partial v}{\partial x}\right) && (2.3)\\
S_{11} &= \frac{\partial u}{\partial x} && (2.4)\\
S_{22} &= \frac{\partial v}{\partial y} && (2.5)
\end{aligned}$$

Following the nondimensionalization provided later in this text for the flow solver, a nondimensional shear rate can be found using

$$\begin{aligned}
S_{12}^* &= \frac{1}{2}\left(\frac{\partial u^*}{\partial y^*} + \frac{\partial v^*}{\partial y^*}\right) && (2.6)\\
S_{11}^* &= \frac{\partial u^*}{\partial x^*} && (2.7)\\
S_{22}^* &= \frac{\partial v^*}{\partial y^*} && (2.8)
\end{aligned}$$

where the nondimensional terms are related to the dimensional terms by

$$S_{12} = S^*_{12}\frac{V_\infty}{L} \tag{2.9}$$

$$S_{11} = S^*_{11}\frac{V_\infty}{L} \tag{2.10}$$

$$S_{22} = S^*_{22}\frac{V_\infty}{L} \tag{2.11}$$

Substituting Equations 2.9 - 2.11 into Equation 2.2 we find

$$S = \frac{V_\infty}{L}S^* \tag{2.12}$$

for the bloodflow cases, $V_\infty = 0.2228$ and $L = 0.004$. Thus for dimensional shear rate $S = 100\text{s}^{-1}$, the corresponding nondimensional shear rate is $S^* \approx 1.79$.

Notice that in the cost function provided in Equation 2.1, if $S^* >> 1$ the contritubtion to the summation is essentially zero whereas if $S^* << 1$ the cost will be very high. In reality, a valid shear distribution may have values near to 1.79 which means that designing to this cost function cannot actually achieve a cost of zero. This actually relaxes the convergence requirements and allows values on the order of 1.0e+00 and even 1.0e+01 to be considered ideal. Furthermore, this function considers the entire distribution of shear rates. This is important because, as stated in Chapter 1, the Newtonian assumption made by many flow solvers is adequate only in the obtaining the shear distribution and not in obtaining the actual values of shear.

Obviously, the situation which truly maximizes the shear rate is to have no stent at all obstructing the flow. Since this is not an option, a side constraint needs to be defined to ensure that the stent has width. Since the shape of the stent is defined by a set of points, it is easy to approximately compute the area of the stent. The side constraint used in this study is defined in equation 2.13 and ensures that the area of the new stent cross-sectional shape must be greater than half the area of the commercially used square cross-sectional stent wires.

$$A > 0.00000001\ \text{mm}^2 \tag{2.13}$$

Governing Equations

The two-dimensional Navier-Stokes equations (provided in full in [10]) are presented below neglecting body forces and external heat:

$$\tfrac{\partial \rho}{\partial t} + \boldsymbol{\nabla} \cdot (\rho \boldsymbol{V}) = 0 \tag{2.14}$$

$$\tfrac{\partial}{\partial t}(\rho \boldsymbol{V}) + \boldsymbol{\nabla} \cdot \rho \boldsymbol{V}\boldsymbol{V} - \boldsymbol{\nabla} \cdot \boldsymbol{\Pi}_{ij} = 0 \tag{2.15}$$

$$\tfrac{\partial E_t}{\partial t} + \boldsymbol{\nabla} \cdot E_t \boldsymbol{V} + \boldsymbol{\nabla} \cdot \boldsymbol{q} - \boldsymbol{\nabla} \cdot (\boldsymbol{\Pi}_{ij} \cdot \boldsymbol{V}) = 0 \tag{2.16}$$

where $\boldsymbol{\nabla}$ is the divergence operator, $\boldsymbol{V}$ is the velocity vector, ρ is the density, E_t is the total energy per unit volume, $\boldsymbol{q} = -k\boldsymbol{\nabla}T$ is the heat transfer (T is the temperature and k is the coefficient of thermal conductivity), and the stress tensor is represented by $\boldsymbol{\Pi}_{ij}$. In the above equations,

$$E_t = \rho\left(e + \frac{u^2 + v^2}{2}\right) \tag{2.17}$$

$$\boldsymbol{\Pi}_{ij} = -p\delta_{ij} + \tau_{ij} \tag{2.18}$$

$$\tau_{ij} = \mu\left[\left(\frac{\partial u_i}{\partial x_j} + \frac{\partial u_j}{\partial x_i}\right) - \frac{2}{3}\delta_{ij}\frac{\partial u_k}{\partial x_k}\right] \tag{2.19}$$

where e is the internal energy per unit mass, u and v are the x and y components of velocity, p is the pressure, δ_{ij} is the Kroenecker delta function, and μ is the coefficient of viscosity.

The implementation uses the following nondimensionalization [10]:

$$\begin{array}{llll} x^* = \frac{x}{L} & y^* = \frac{y}{L} & t^* = \frac{t}{\frac{L}{V_\infty}} & \\ u^* = \frac{u}{V_\infty} & v = \frac{v}{V_\infty} & \mu^* = \frac{\mu}{\mu_\infty} & \\ \rho^* = \frac{\rho}{\rho_\infty} & p^* = \frac{p}{\rho_\infty V_\infty^2} & T^* = \frac{T}{T_\infty} & e^* = \frac{e}{V_\infty^2} \end{array} \tag{2.20}$$

where L is the reference length, the subscript $_\infty$ represents freestream conditions, and the Reynolds number is given by $Re_L = \frac{\rho_\infty V_\infty L}{\mu_\infty}$. Substituting these nondimensionalized variables back into equations 2.14 - 2.16 and rewriting in vector form gives:

$$\frac{\partial \boldsymbol{Q}^*}{\partial t^*} + \frac{\partial \boldsymbol{f}_i^*}{\partial x^*} + \frac{\partial \boldsymbol{g}_i^*}{\partial y^*} = \frac{\partial \boldsymbol{f}_v^*}{\partial x^*} + \frac{\partial \boldsymbol{g}_v^*}{\partial y^*} \tag{2.21}$$

where Q is the vector of conservative variables given by

$$\boldsymbol{Q}^* = \begin{bmatrix} \rho^* \\ \rho^* u^* \\ \rho^* v^* \\ E_t^* \end{bmatrix} \tag{2.22}$$

f_i and g_i are the inviscid fluxes given by

$$\boldsymbol{f}_i^* = \begin{bmatrix} \rho^* u^* \\ \rho^* u^{*2} + p^* \\ \rho^* u^* v^* \\ (E_t^* + p^*) u^* \end{bmatrix} \tag{2.23}$$

$$\boldsymbol{g}_i^* = \begin{bmatrix} \rho^* v^* \\ \rho^* u^* v^* \\ \rho^* v^{2*} + p^* \\ (E_t^* + p^*) v^* \end{bmatrix} \tag{2.24}$$

and f_v and g_v are the viscous fluxes given by

$$\boldsymbol{f}_v^* = \begin{bmatrix} 0 \\ \tau_{xx}^* \\ \tau_{xy}^* \\ u^*\tau_{xx}^* + v^*\tau_{xy}^* - q_x^* \end{bmatrix} \tag{2.25}$$

$$\boldsymbol{g}_v^* = \begin{bmatrix} 0 \\ \tau_{xy}^* \\ \tau_{yy}^* \\ u^*\tau_{xy}^* + v^*\tau_{yy}^* - q_y^* \end{bmatrix} \tag{2.26}$$

$$\tau_{xx}^* = \frac{2\mu^*}{3Re_L}\left(2\frac{\partial u^*}{\partial x^*} - \frac{\partial v^*}{\partial y^*}\right) \tag{2.27}$$

$$\tau_{yy}^* = \frac{2\mu^*}{3Re_L}\left(2\frac{\partial v^*}{\partial y^*} - \frac{\partial u^*}{\partial x^*}\right) \tag{2.28}$$

$$\tau_{xy}^* = \frac{\mu^*}{Re_L}\left(\frac{\partial u^*}{\partial y^*} + \frac{\partial v^*}{\partial x^*}\right) \tag{2.29}$$

$$q_x^* = -\frac{\mu^*}{(\gamma-1)M_\infty^2 Re_L Pr}\frac{\partial T^*}{\partial x^*} \tag{2.30}$$

$$q_y^* = -\frac{\mu^*}{(\gamma-1)M_\infty^2 Re_L Pr}\frac{\partial T^*}{\partial y^*} \tag{2.31}$$

The Mach number and the nondimensionalized forms of the equations of state are given by:

$$
\begin{aligned}
M_\infty &= \frac{V_\infty}{\sqrt{\gamma R T_\infty}} && (2.32)\\
p^* &= (\gamma - 1)\rho^* e^* && (2.33)\\
T^* &= \frac{\gamma M_\infty^2 p^*}{\rho^*} && (2.34)
\end{aligned}
$$

where R is the gas constant and γ is the ratio of specific heats.

Numerical Formulation

The nondimesionalized compressible Navier-Stokes equations given by 2.21 are discretized in a point Gauss-Siedel implicit node-centered finite volume scheme which is 2nd order accurate in space, 1st order accurate in time. The scheme uses Van Leer flux vector splitting for the inviscid fluxes, central differencing for the viscous fluxes, and characteristic variable boundary conditions. The discretized equation for the i^{th} node is:

$$A_i \frac{\Delta Q_i}{\Delta t_i} + \sum_j \frac{\partial F_i}{\partial Q_j} \Delta Q_j = -\sum_j F_{ij} \cdot \hat{n}_{ij} + \sum_j F_{v_{ij}} \cdot \hat{n}_{ij} \qquad (2.35)$$

where ΔQ is the change in Q for node i between the n and $n+1$ timesteps, Δt_i is the local timestep for node i, $\frac{\partial F_i}{\partial Q_j}$ are derivatives of the inviscid flux at node i with respect to Q, F_{ij} and $F_{v_{ij}}$ are the inviscid and viscous fluxes across the face between nodes i and j, and $\hat{n}_{ij}$ is the unit vector normal to the control volume face between nodes i and j. In two dimensions, A_i is the area of the control volume around node i and S_{ij} is the length of the vector that forms the face between nodes i and j.

Timestep Calculation

The local timestep for node i is taken to be the area of the control volume around i divided by the sum over all edges around i of the largest eigenvalue:

$$\Delta t_i = \frac{A_i}{\sum_j (|\bar{U}| + c)l} \tag{2.36}$$

where $\bar{U} = u\hat{n}_x + v\hat{n}_y$ is the contravariant velocity, c is the local speed of sound, and l is the length of the vector n, which is normal to the face between i and j.

Van Leer Flux Vector Splitting

The inviscid flux in equation 2.35 is computed using Van Leer flux vector splitting. The flux is split into two components, F^+ and F^- such that the following criteria are satisfied [10]:

1. $F(Q) = F^+(Q) + F^-(Q)$.
2. $\frac{\partial F^+}{\partial Q}$ contains all eigenvalues ≥ 0 and $\frac{\partial F^-}{\partial Q}$ contains all eigenvalues ≤ 0.
3. $F^{\pm}$ must be continuous with $F^+(Q) = F(Q)$ for $\bar{U} \geq c$ and $\frac{\bar{U}}{c} \geq 1$ and $F^-(Q) = F(Q)$ for $\bar{U} \leq -c$ and $\frac{\bar{U}}{c} \leq -1$
4. The components of F^+, F^- exhibit the same symmetry that F exhibits (if $F(\bar{U}) = \pm F(-\bar{U})$, then $F^+ = \pm F^-(-\bar{U})$).
5. The Jacobians $\frac{\partial F^{\pm}}{\partial Q}$ are continuous.
6. The Jacobians $\frac{\partial F^{\pm}}{\partial Q}$ must have one eigenvalue vanish for $|M| < 1$.
7. $F^{\pm}$ must be a polynomial in Mach number of lowest possible order.

The equations for Van Leer flux vector splitting are given below [11].

$$F^{\pm} = \begin{bmatrix} \pm\frac{1}{4}\rho c\left(\frac{\bar{U}}{c} \pm 1\right)^2 \\ F_1^{\pm}\left(\frac{\hat{n}_x}{\gamma}\left(-\bar{U} \pm 2c\right) + u\right) \\ F_1^{\pm}\left(\frac{\hat{n}_y}{\gamma}\left(-\bar{U} \pm 2c\right) + v\right) \\ F_1^{\pm}\left[\frac{-(\gamma-1)\bar{U}^2 \pm 2(\gamma-1)\bar{U}c + 2c^2}{\gamma^2-1} + \frac{u^2+v^2}{2}\right] \end{bmatrix} \tag{2.37}$$

where $\bar{U}$ is the contravariant velocity $\bar{U} = u\hat{n}_x + v\hat{n}_y$ and c is the local speed of sound. Thus, for a given face between nodes i and j, the inviscid flux is

$$F_{ij} \cdot \hat{n}_{ij} = F^{+}(Q_l) + F^{-}(Q_r) \tag{2.38}$$

Q_l and Q_r are the Q values on the left and right, respectively, and are determined by the direction of the normal. For instance, for first order spatial accuracy when $\hat{n}$ points in the direction from node i to node j, $Q_l = Q_i$ and $Q_r = Q_j$. For second order spatial accuracy, the gradients at the nodes are involved, resulting in $Q_l = Q_i + \nabla Q_i \cdot (\vec{x}_m - \vec{x}_i)$ and $Q_r = Q_j + \nabla Q_j \cdot (\vec{x}_m - \vec{x}_j)$, where $\vec{x}_i$, $\vec{x}_j$ are the coordinate vectors associated with nodes i and j respectively and $\vec{x_m}$ is the coordinate vector of the midpoint of the edge between i and j.

Boundary Conditions

The computation of the fluxes requires information on the left and the right side of the face between the nodes. These left and right states are easy to identify inside the mesh, but this is difficult at the boundaries. For flux computation on a given boundary segment, Q_l is taken to be an average of the Q values at the boundary nodes and Q_r is taken to be the Q values at some "ghost" node just outside the boundary. Characteristic variable boundary conditions are used in this implementation to find the appropriate Q values for this ghost node. Bloodflow is characterized by very low Mach numbers, so the boundary conditions needed for the cases are: subsonic inflow, subsonic outflow, impermeable surface, and symmetry plane. In the following discussion of boundary conditions, variables with a subscript $_i$ refer to values at physical nodes, variables with the subscript $_\infty$ refer to the values at freestream, the subscript $_b$ refers to the value at the ghost node, and the subscript $_0$ refers to an arithmetic average of the values at the physical and ghost nodes. The convention used in this implementation is for outward pointing boundary normals. The eigenvalues are $\lambda_1 = \lambda_2 = \theta$, $\lambda_3 = \theta + c$, and $\lambda_4 = \theta - c$, where θ is the contravariant velocity: $\theta = u\hat{n}_x + v\hat{n}_y$.

Subsonic Inflow

Subsonic inflow is characterized by $\lambda_{1,2,4} < 0$ and $\lambda_3 > 0$. Following the derivation in [12], the boundary values are given by the following equations:

$$p_b = \frac{1}{2}\left[p_\infty + p_i - \rho_0 c_0 \left\{\hat{n}_x(u_\infty - u_i) + \hat{n}_y(v_\infty - v_i)\right\}\right] \tag{2.39}$$

$$\rho_b = \rho_\infty - \frac{p_\infty - p_b}{c_0^2} \tag{2.40}$$

$$u_b = u_\infty - \hat{n}_x \frac{p_\infty - p_b}{\rho_0 c_0} \tag{2.41}$$

$$v_b = v_\infty - \hat{n}_y \frac{p_\infty - p_b}{\rho_0 c_0} \tag{2.42}$$

Subsonic Outflow

Subsonic outflow is characterized by $\lambda_{1,2,3} > 0$ and $\lambda_4 < 0$. Following the derivation in [12], which takes pressure to be the one piece of information that comes from outside the domain, the boundary values can be given by the following equations:

$$
\begin{aligned}
p_b &= p_\infty && (2.43)\\
\rho_b &= \rho_i + \frac{p_b - p_i}{c_0^2} && (2.44)\\
u_b &= u_i - \hat{n}_x \frac{p_b - p_i}{\rho_0 c_0} && (2.45)\\
v_b &= v_i - \hat{n}_y \frac{p_b - p_i}{\rho_0 c_0} && (2.46)
\end{aligned}
$$

For internal flow problems p_∞ refers to a specified back pressure which preserves the desired pressure drop across the domain. In all other cases, it refers to the pressure at the freestream conditions.

Solid Wall Conditions

An inviscid solid wall is characterized by $\lambda_{1,2} = 0$, $\lambda_3 > 0$ and $\lambda_4 < 0$. This condition is also called a “slip” condition because it allows flow tangential to the boundary but does not allow any flow through the boundary. The resulting equation set is:

$$
\begin{aligned}
p_b &= p_i + \rho_0 c_0 \left(\hat{n}_x u_i + \hat{n}_y v_i\right) && (2.47)\\
\rho_b &= \rho_i + \frac{p_b - p_i}{c_0^2} && (2.48)\\
u_b &= u_i - \hat{n}_x \frac{p_b - p_i}{\rho_0 c_0} && (2.49)\\
v_b &= v_i - \hat{n}_y \frac{p_b - p_i}{\rho_0 c_0} && (2.50)
\end{aligned}
$$

The viscous solid wall condition (also called a “no-slip” condition) is computed in the same way as the inviscid solid wall condition except that u and v are identically zero at the boundary.

Symmetry Plane

A symmetry plane condition is used in cases where the flow is assumed to be symmetric about a plane and thus the problem size can be reduced in half. All of the meshes created with this condition are completely structured, so every symmetry plane node is connected to exactly one non-symmetry plane node. Let the subscript $_i$ here refer to the values at this non-symmetry node. Then the values at the boundary are given by:

$$p_b = p_i \tag{2.51}$$

$$\rho_b = \rho_i \tag{2.52}$$

$$u_b = V_i - (V_i \cdot \hat{n})\, \hat{n}_x \tag{2.53}$$

$$v_b = V_i - (V_i \cdot \hat{n})\, \hat{n}_y \tag{2.54}$$

Mesh Movement

In order to optimize the cross-sectional shape of the stent, two operations need to be performed on the mesh:

1. To reduce the total number of design variables, the boundary representing the stent needs to be parametrized.
2. Based on the above parametrization, the mesh needs to be moved to the new stent shape proposed by the optimizer.

This implementation uses Hick-Henne functions for parametrization and linear elastic smoothing for the mesh movement.

Hicks-Henne Parametrization

The Hicks-Henne shape functions are a set of n sine waves with specified positions for the maximum of each wave in the interval $(0, 1)$ [13]. Let x_{M_i} be the specified location for the maximum of the i^{th} function and let its position be defined in the following way:

$$x_{M_i} = 0.5\,(1 - \cos(\theta_i)) \tag{2.55}$$

where $\theta_i = \frac{\pi i}{n+1}$. This produces a distribution of x_{M_i}'s that is denser towards the leading and trailing edges. The Hicks-Henne functions are then defined by:

$$\begin{aligned} b_i(x) &= \sin^4(\pi x^{m_i}) && (2.56) \\ m_i &= \frac{\ln 0.5}{\ln x_{M_i}} && (2.57) \\ & && (2.58) \end{aligned}$$

Any new shape for the boundary can be obtained by adding a linear combination of the n Hicks-Henne functions to the initial shape. In this case the n weights of the linear combination become the n design variables that the optimization routine will find. As can be seen in figure 2.4, although the distribution of the x_{M_i}s is symmetric over the interval, the resulting functions are not symmetric. For instance, the peak for the first and last function is the same distance from the boundary of the interval, however the sine wave for the first function has a greater width than the sine wave for the last function. This type of parametrization favors an airfoil-like shape. It is also important to note that this parametrization is based on the initial mesh and requires that every function evaluation for the design process start from the exact same mesh.

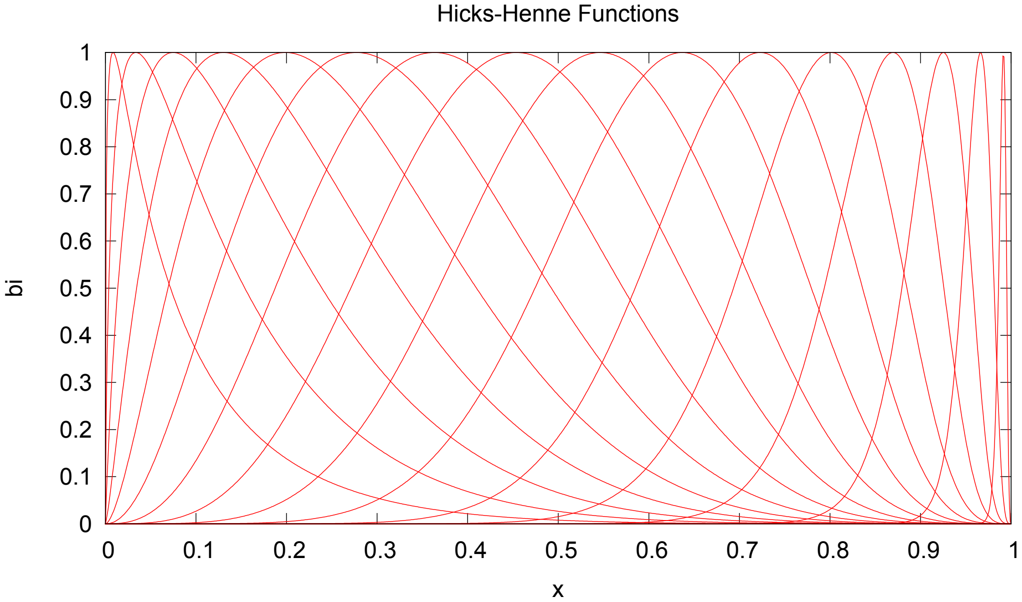

Figure 2.4 Hicks-Henne Shape Functions for 16 Design Variables

Linear Elastic Smoothing

Linear-elastic smoothing is a robust method of mesh movement which smoothes the interior points of a mesh when the boundary has been moved or deformed [14]. Linear-elastic smoothing can perform very large deformations in both viscous and inviscid meshes while maintaining good spacings in the boundary layer. This method is ideal for design optimization since it can handle large deformations of the mesh and it can also be used to find mesh sensitivity derivatives for gradient-based optimization methods[14].

The differential equations governing linear-elastic smoothing in two dimensions are presented below [14].

$$\frac{\partial}{\partial x}\left[\alpha_1\frac{\partial u}{\partial x}\right]+\frac{\partial}{\partial y}\left[\alpha_2\frac{\partial u}{\partial y}\right]+\frac{\partial}{\partial x}\left[\alpha_3\frac{\partial v}{\partial y}\right]+\frac{\partial}{\partial y}\left[\alpha_2\frac{\partial v}{\partial x}\right] = 0 \tag{2.59}$$

$$\frac{\partial}{\partial x}\left[\alpha_2\frac{\partial v}{\partial x}\right]+\frac{\partial}{\partial y}\left[\alpha_1\frac{\partial v}{\partial y}\right]+\frac{\partial}{\partial x}\left[\alpha_2\frac{\partial u}{\partial y}\right]+\frac{\partial}{\partial y}\left[\alpha_3\frac{\partial u}{\partial x}\right] = 0 \tag{2.60}$$

where

$$\alpha_1 = \frac{E(1-\nu)}{(1+\nu)(1-2\nu)} \tag{2.61}$$

$$\alpha_2 = \frac{E}{2(1+\nu)} \tag{2.62}$$

$$\alpha_3 = \frac{E\nu}{(1+\nu)(1-2\nu)} \tag{2.63}$$

$$\tag{2.64}$$

In the above equations, the solution vector $[u, v]^\intercal$ defines the displacement at each node [14], E represents Young's Modulus and is taken to be the element aspect ratio, and ν represents Poisson's ratio and is taken to be 0.20. The resulting system of equations is solved using a point implicit finite volume method.

CHAPTER 3

VALIDATION

The goal of this section is to show that the solver matches benchmark analytical solutions for viscous flow and that it matches published computational results for blood flow. The viscous terms and boundary conditions will be verified by examining the Blasius equation for laminar flow over a flat plate and Couette flow. The blood flow cases will consider flow through a stented artery for a square, semi-circular, and streamlined shaped stent cross-section.

Laminar Flow Along a Flat Plate

The first validation case considered is laminar flow along an infinitely thin flat plate. This case was chosen because the nature of the flow is characterized by the viscous terms and so it will verify that the code can simulate viscous flow. The Blasius equation, shown in equation 3.1, takes the boundary-layer equations (2 partial differential equations) and combines them through the dimensionless coordinate η into one ordinary differential equation [15].

$$f(\eta)f''(\eta) + 2f'''(\eta) = 0 \tag{3.1}$$

$$\eta = y\sqrt{\frac{U_\infty}{\nu x}} \tag{3.2}$$

Furthermore, the velocity profile can be obtained from the relation

$$\frac{u}{U_\infty} = f'(\eta) \tag{3.3}$$

A structured mesh with viscous spacing was created which is rectangular in shape. The sides and top have a farfield condition and the bottom of the plate is split into 3 sections: a flat plate of unity length and viscous wall condition with a region of inviscid wall conditon on either side. A Reynold's number of 10000, Mach number of 0.8, and normal freestream conditions for air were used for this case.

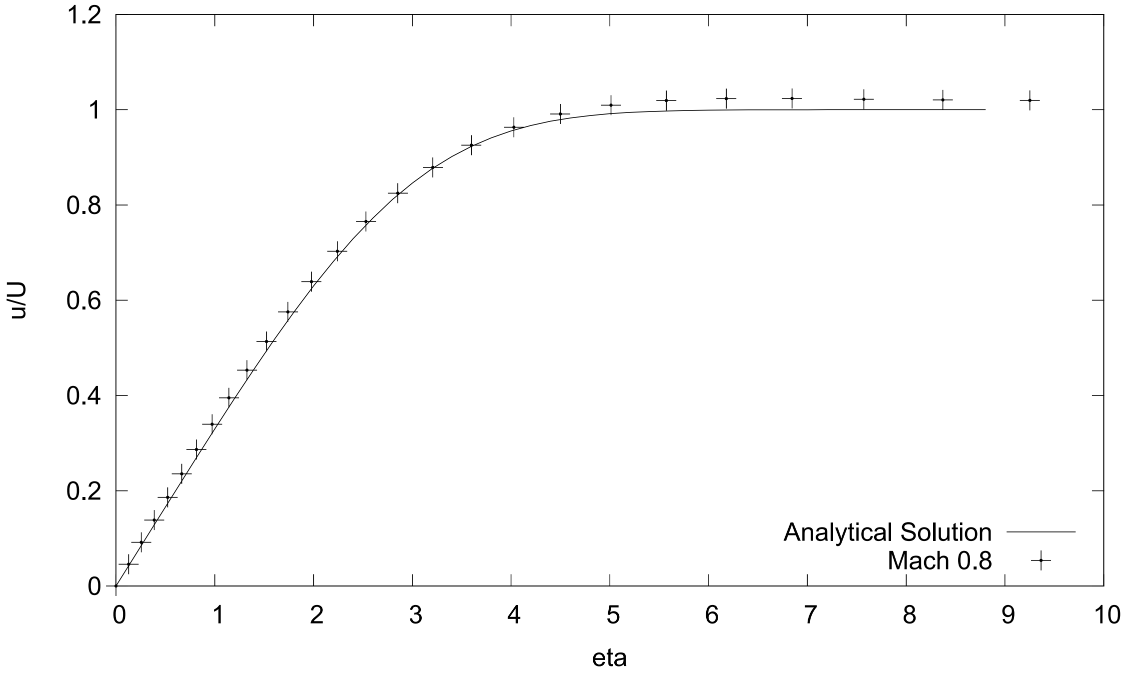

Figure 3.1 Comparison of Profiles for Blasius Test Case

Figure 3.1 shows the comparison of the computed solution to the analytical solution of the Blasius equation. The analytical solution used is the numerical solution to the Blasius equation found by L. Howarth [15]. The computed solution is found using the velocities in a column of the mesh located at $\frac{3}{4}$ of the length of the plate. The computed solution reaches a value slightly higher than 1 at freestream. This can be attributed to the fact that the abrupt transition between the inviscid wall condition and the viscous wall condition at the leading edge of the plate causes the velocity to speed up slightly. Other than this overshoot, the computed solution agrees well with the analytical solution.

Couette Flow

The second validation case is Couette flow, which is flow between two parallel surfaces in which the distance h between the surfaces is small in comparison to the length of the channel. This case was chosen because it is the two-dimensional analog of Poiseuille flow, which is often used to model the flow of blood in blood vessels. Couette flow is not only viscous dominated, but also highly dependent on the boundary conditions. Successful execution of this case will verify that the boundary conditions and the freestream conditions are adequate for modeling blood flow problems.

In Couette flow, the direction of flow is in the x-direction only, causing pressure to become a function of x only and velocity to become a function of y only [16]. The Navier Stokes equations then reduce to:

$$0 = -\frac{dp}{dx} + \mu \frac{d^2 u}{dy^2} \tag{3.4}$$

Integrating this twice and applying the conditions $u(0) = u(h) = 0$, the velocity can expressed as a function of y:

$$u(y) = -\frac{1}{2\mu}\frac{dp}{dx} y\,(h - y) \tag{3.5}$$

Dividing by a reference velocity and substituting $P = -\frac{h^2}{2\mu U}\frac{dp}{dx}$ produces the nondimensionalized velocity profile:

$$\frac{u(y)}{U} = P\frac{y}{h}\left(1 - \frac{y}{h}\right) \tag{3.6}$$

Thus when the pressure drop through the channel, h, and μ are known, the velocity profile can be exactly computed using the above equation.

The freestream conditions for the blood flow cases were derived from the density and viscosity of blood (assumed to be constant) using Couette flow and the equations of state. They are listed in Table 3.1.

Table 3.1 Freestream Conditions for Blood Flow Cases

Variable	Value	Unit of Measure
Density	1060·0	kg/m^3
Viscosity	0·0035	kg/m·s
Reference Length	0·004	m
Temp	0·0442482	degree K
Velocity	0·2228773585	m/s
Inlet Pressure	13463·89	Pa
Back Pressure	13424·808455	Pa
Mach Number	0·052853	(dimensionless)
Reynolds Number	270·0	(dimensionless)

Three structured meshes were created for this test case with 32×32, 64×64, and 128×128 evenly spaced points. Each mesh extends from -50 mm to 50.2 mm in the x-direction and from 0 to a height of 4 mm in the y-direction. The profiles for the computed solutions were taken at the center column in the mesh. Figure 3.2 compares the velocity profiles from the computed solutions to the analytical profile.

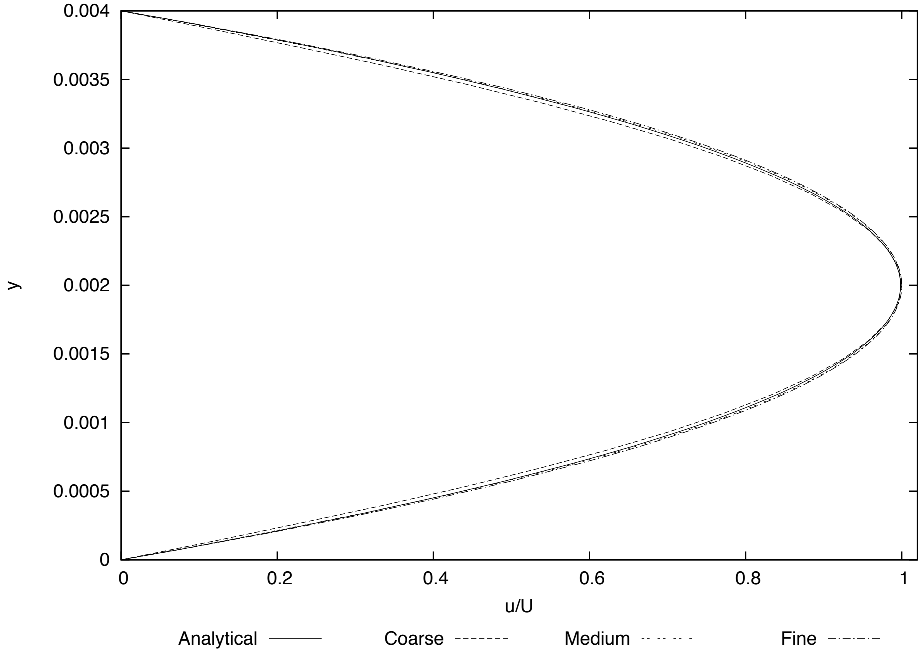

Figure 3.2 Comparison of Velocity Profiles for Couette Flow:Full Profile

Since Couette flow is naturally symmetric about the centerline of the channel, the problem can be cut in half using a symmetry condition. Three structured meshes were created which again extended from -50 to 50.2 mm in the x-direction but only extended from 0 to 2 mm in the y-direction. These three meshes had the same spacings as those before, but only half the total number of points. Figure 3.3 shows the comparison of the computed solutions to that of the analytical solution found for the same flow conditions. In both cases, as the mesh is refined, the computed solution more closely matches the analytical solution.

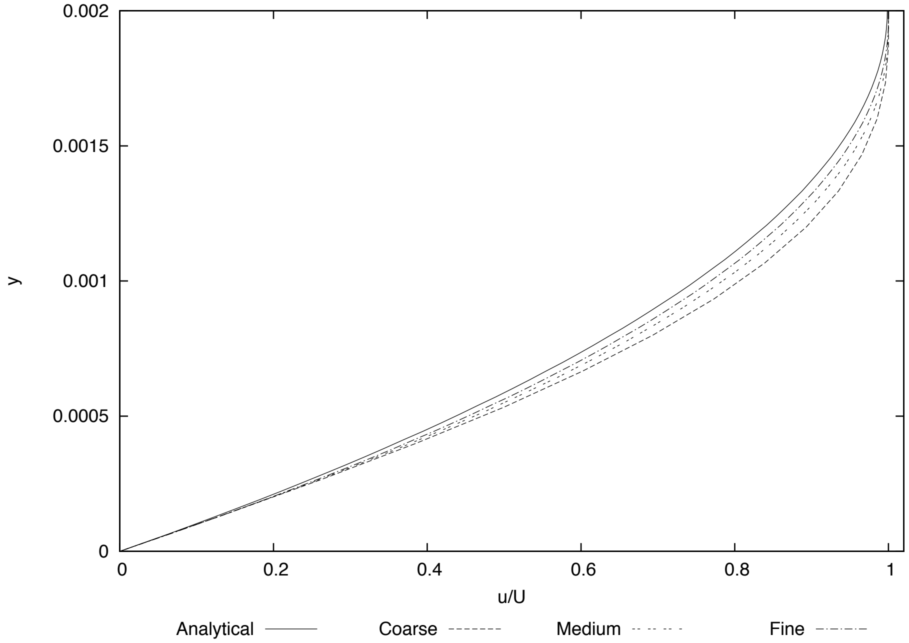

Figure 3.3 Comparison of Velocity Profiles for Couette Flow: Symmetry Plane Condition

It is worth noting that the reference velocity U for the analytical profile was taken to be the freestream velocity whereas for the computed solutions it was taken to be the maximum velocity in the mesh at the column of x values. The reason for this discrepancy is that the characteristic inflow condition is not the ideal boundary condition for this type of flow. While the appropriate pressure is achieved at the outflow, the inflow pressure is not exactly matched. A total pressure condition for the inflow boundary would help enforce the correct pressure drop and implementing such a condition is intended for the future.

Stent Validation Cases

This section compares the results of simulating flow thorugh stented blood vessels to results from other studies. Three geometries are considered: rectangular, semi-circular, and streamlined stent cross-sectional shapes. The parameters for the geometries are those used by Chen *et al.*, in which the height h of each stent is 0.1 mm, the width d of the rectangular and semi-circular stents is 0.2 mm and the width of the streamlined stent is 0.5 mm, and the diameter of the blood vessel is 4.0 mm [17]. The shape of the streamlined stent is defined by the equation:

$$R(z) = 0.1e^{-z^2} \tag{3.7}$$

where $z = d/h$ $(-2.5 \leq z \leq 2.5)$. Jimenez and Davies also studied the rectangular and semi-circular shapes using one stent ring, whereas Chen *et al.* used five stent rings. In order to compare to both studies, the meshes were created with only one stent ring. The viscous spacing used is small enough to resolve the recirculation zones. The contours of the velocity for each of the shapes can be seen in Figures 3.4 - 3.6.

Chen *et al.* compared the length of the recirculation zone to the height of the stent for each of their 5 stent rings. Their results can be found in Figure 3.7, in which P1-P5 represent the positions of the 5 stent rings and $\frac{L}{h}$ represents the ratio of recirculation length to stent height. Jimenez and Davies also studied the rectangular and semi-circular stents and found $\frac{L}{h}$ for the case of one stent ring to be approximately 0.845 for the rectangular stent and 0.47 for the semi-circular stent. The results obtained here consider the case of only one stent ring and $\frac{L}{h}$ was found to be approximately 0.8 for the rectangular stent and 0.48 for the semi-circular stent. These values correspond well with the results of first stent right of the Chen study as well as to the values found by Jimenez and Davies. The streamlined stent had no observable recirculation, which also corresponds well to the results of $\frac{L}{h} < 0.0015$ obtained by Chen *et al.*

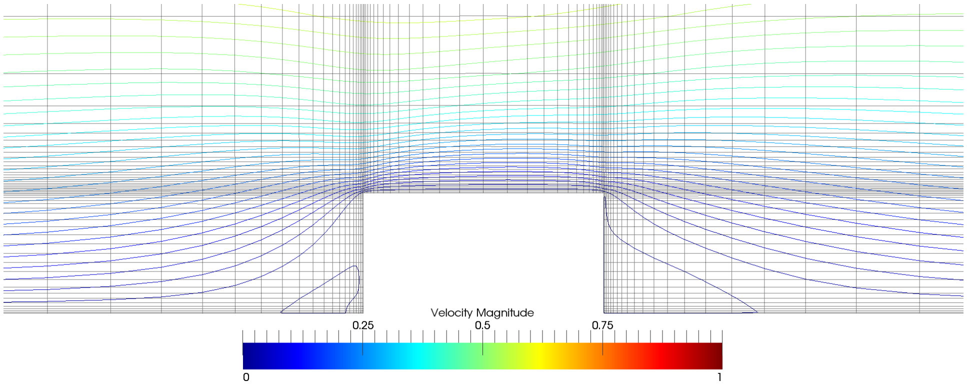

Figure 3.4 Contours of Velocity for the Rectangular Stent

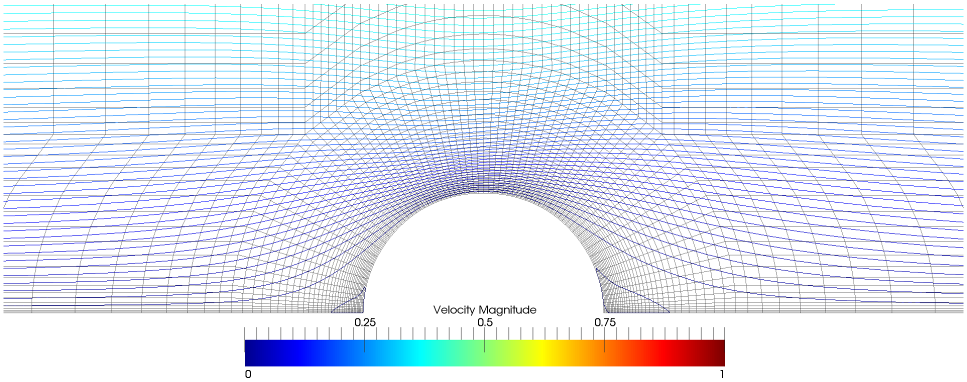

Figure 3.5 Contours of Velocity for the Semi-Circular Stent

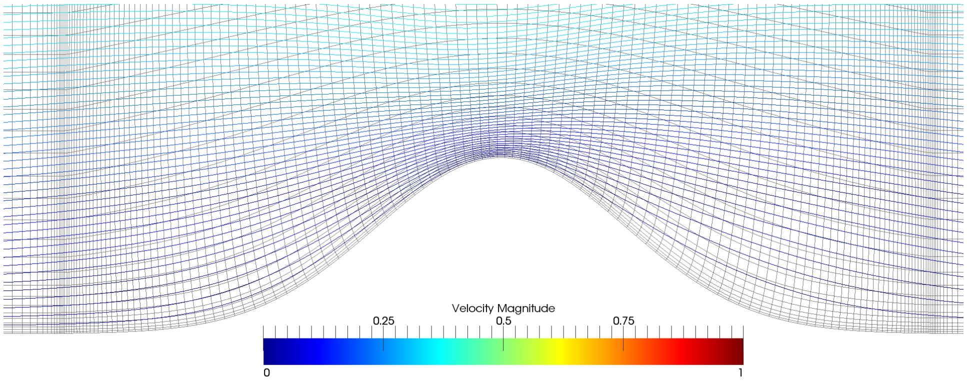

Figure 3.6 Contours of Velocity for the Streamlined Stent

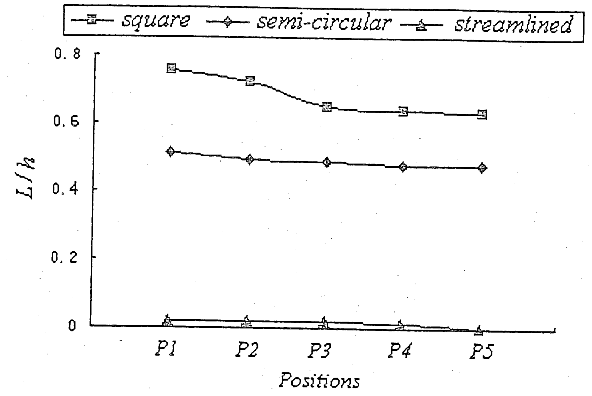

Figure 3.7 Effect of Cross-Sectional Shape on the Length of Recirculation Zones

Jimenez and Davies also studied the profiles of WSS and shear rate for the rectangular and semi-circular stents with varying aspect ratios. Their results can be seen in Figure 3.8, in which part (a) shows the results for the rectangular stent, part (b) shows the results for the semi-circular stent, and the dashed line in each section corresponds to the 2:1 aspect ratio studied here. Figures 3.9 and 3.10 show the distribution of shear rate in the vicinity of the rectangular and semi-circular stents obtained from the computed results. The profile for the rectangular stent matches very well with the results obtained by Jimenez and Davies. The profile for the semi-circular stent achieved a shape similar to the profile obtained by Jimenez and Davies, however the values do not match. This can be attributed to the fact that Jimenez and Davies are using a blood vessel that is 3 mm in diameter and 19.2 mm in length, which may not be long enough to sufficiently establish the inlet velocity profile. Also, they do not provide much detail as to the resolution of their meshes and since this shape is naturally more streamlined than the rectangle, there may not be sufficient resolution for the shear profile to fully develop.

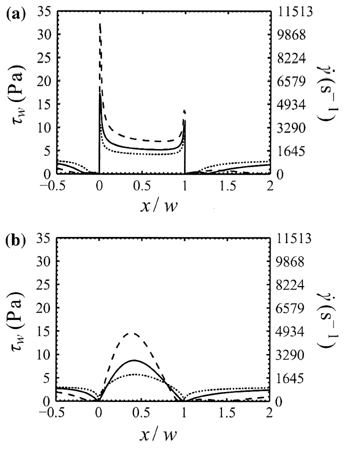

Figure 3.8 WSS and Shear Rate Distributions Obtained by Jimenez and Davies for Rectangular and Semi-Circular Stent Shapes

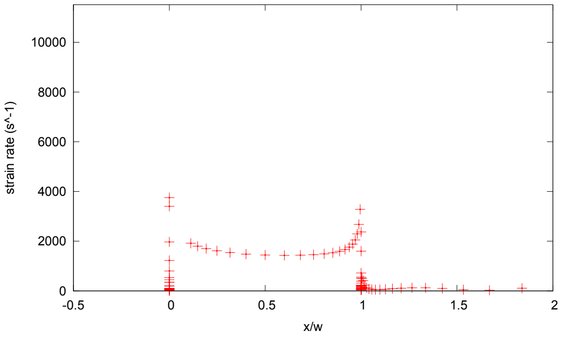

Figure 3.9 Computed WSS Distribution for Rectangular Stent Shape

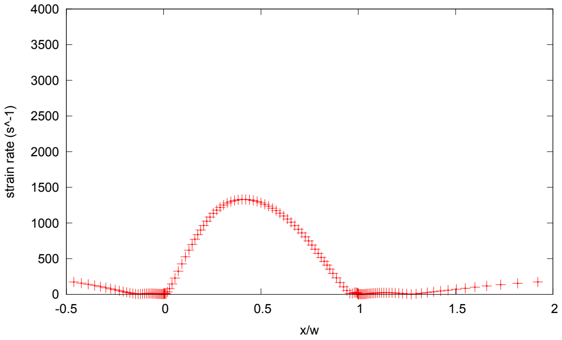

Figure 3.10 Computed WSS Distribution for Semi-Circle Stent Shape

CHAPTER 4

RESULTS

The Hicks-Henne parametrization changes the shape of an existing mesh to obtain the new desired shape. Four different initial shapes were chosen to examine the dependency of the final optimized shape on the initial shape: an elliptical shape, the exponential shape defined by equation 3.7, an airfoil shape, and a flat plate. It is important to note that since the new shape depends on the distribution of the initial mesh, it is possible (and in fact probable) that the optimizer will request a set of design variables which produces a bad mesh. In such a case, the solver will return a cost of 1.0e+15, which is orders of magnitude higher than the cost for any valid mesh. The results in this chapter show only the valid meshes created in the design process.

The initial meshes created have viscous spacing small enough to resolve the recirculation zones and the points on the stent are clustered towards the front and back of the stent. The mesh for the exponential shaped stent can be seen in Figure 3.6. Figures 4.1, 4.2, and 4.3 show the meshes for the elliptical, airfoil, and flat initial stent shapes respectively.

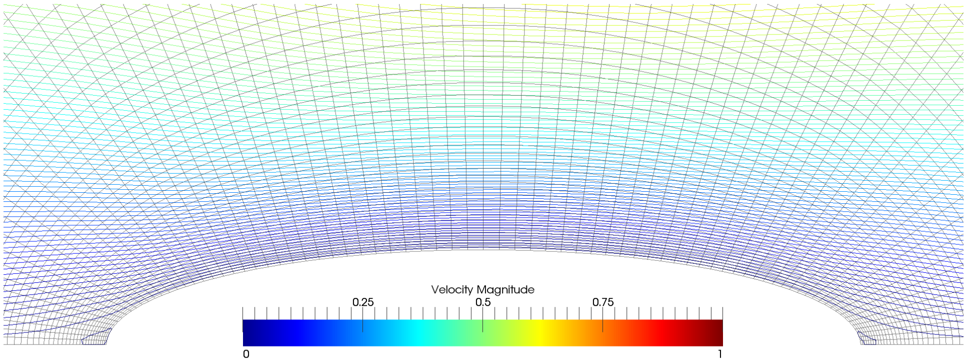

Figure 4.1 Contours of Velocity for Elliptical Shaped Stent

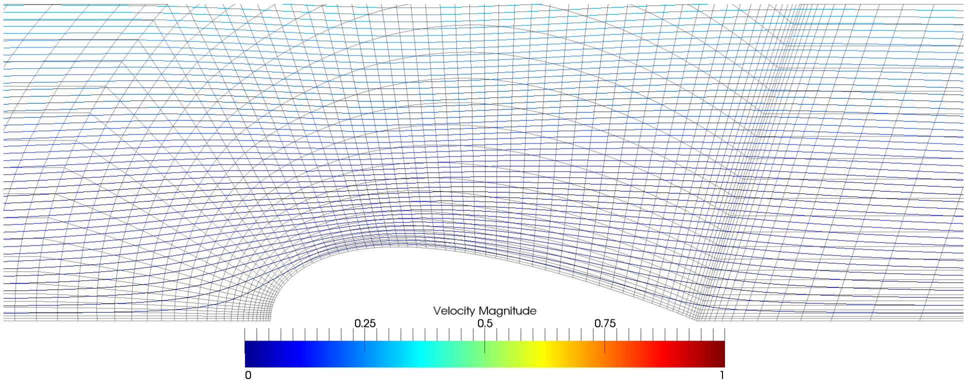

Figure 4.2 Contours of Velocity for Airfoil Shaped Stent

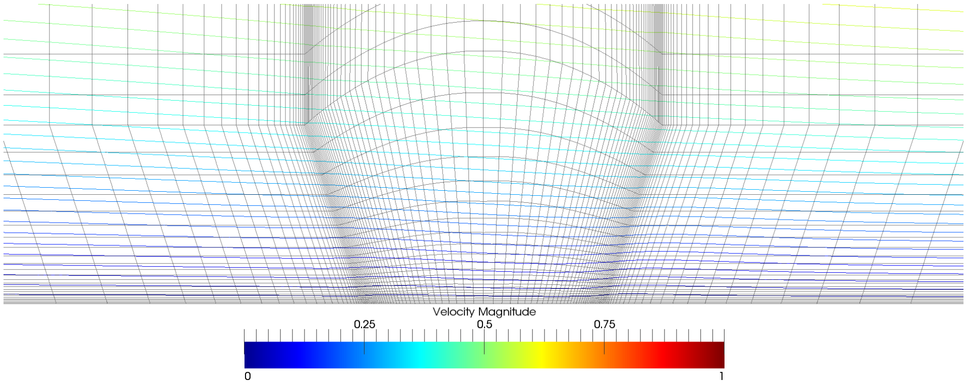

Figure 4.3 Contours of Velocity for Flat Stent

Design of the Elliptical Shaped Stent

The elliptical shape was chosen because it is in a middle position between the ideal unstented case and the extreme semi-circle case. The design process was performed using 8, 12, and 15 design variables as a convergence study and to observe the effect of an even versus an odd number of design variables on the resulting shape.

8 Design Variables

Figures 4.4 - 4.8 show the first 5 valid meshes created in the design process using the elliptical shaped stent and 8 design variables. These images show variations of 2 distinct shapes.

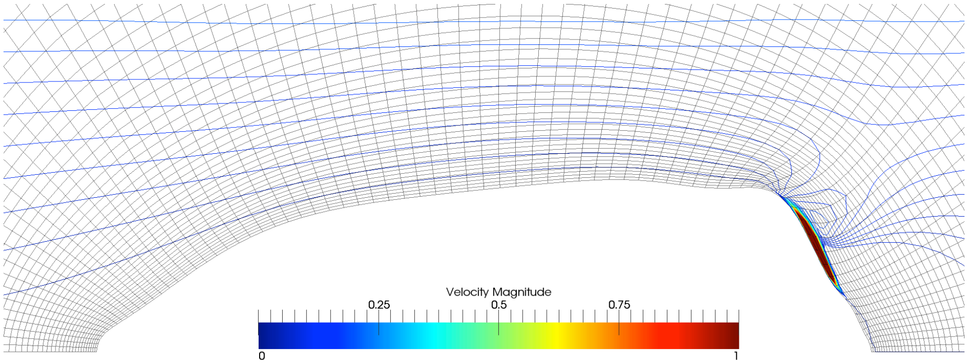

Figure 4.4 Elliptical Shape Design With 8 Design Variables: Iteration 5

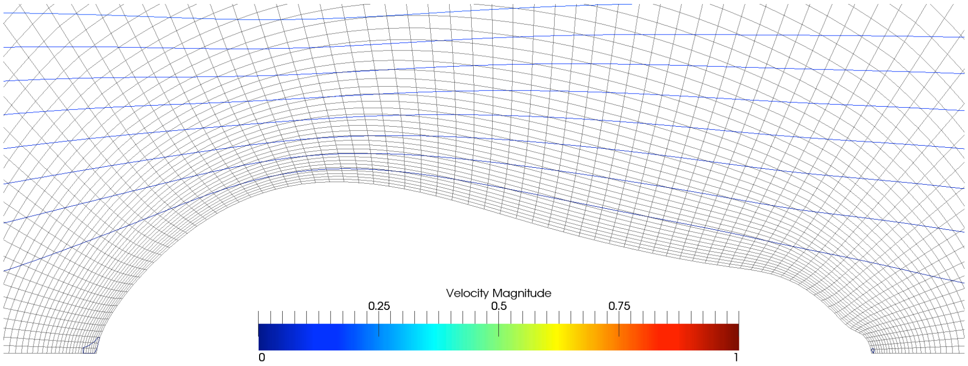

Figure 4.5 Elliptical Shape Design With 8 Design Variables: Iteration 7

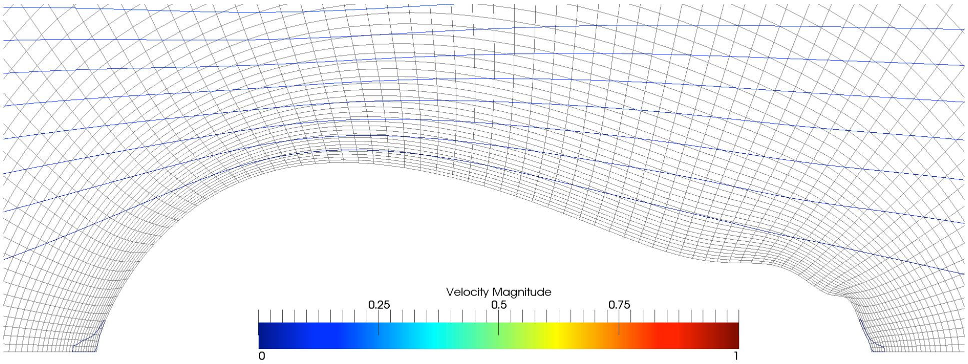

Figure 4.6 Elliptical Shape Design With 8 Design Variables: Iteration 17

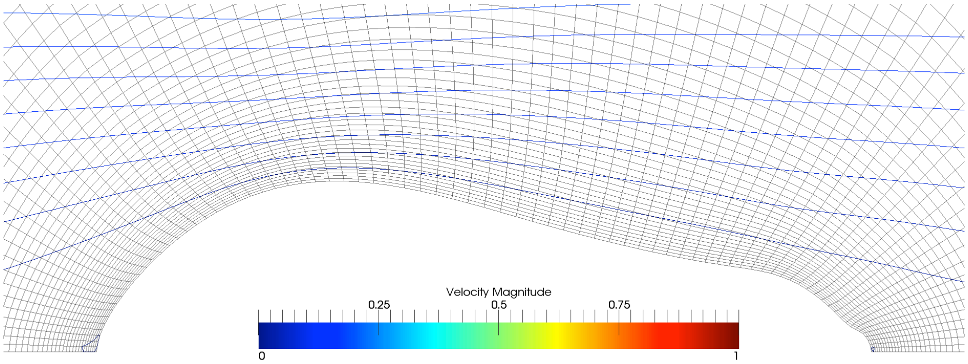

Figure 4.7 Elliptical Shape Design With 8 Design Variables: Iteration 19

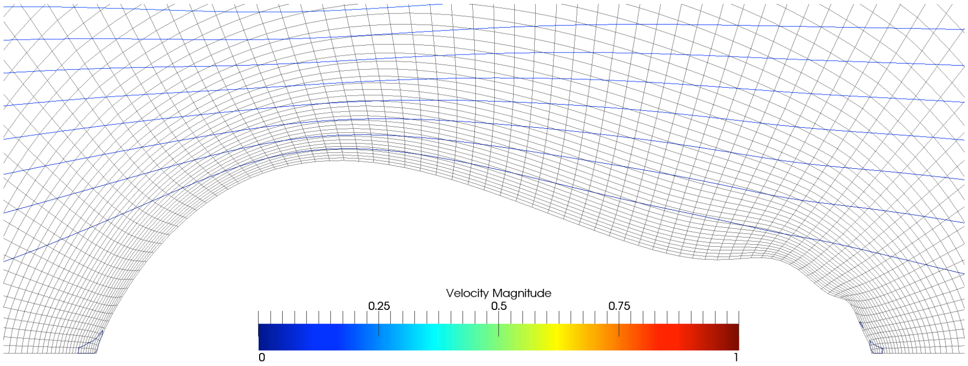

Figure 4.8 Elliptical Shape Design With 8 Design Variables: Iteration 22

Figures 4.9 - 4.11 show the final 3 meshes produced in the design process. These images show that Dakota is optimizing toward the shape initially identified by 5^{th} function evaluation (shown in Figure 4.4). This shape has a region of very high velocity on the back side of the stent and also has a very large recirculation zone behind the stent.

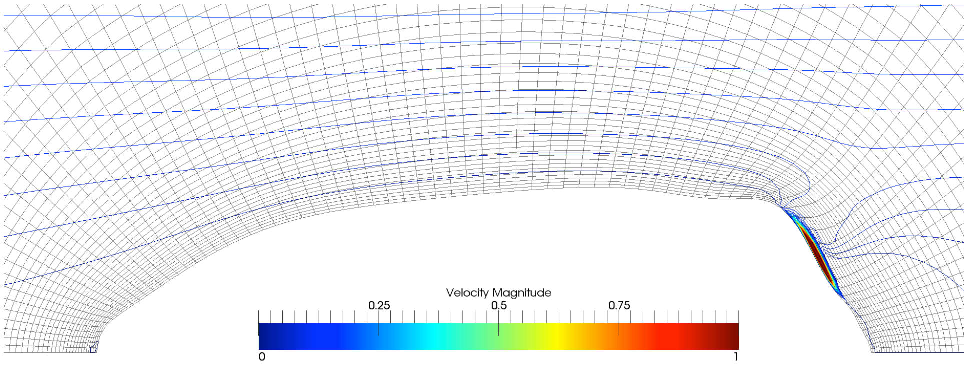

Figure 4.9 Elliptical Shape Design With 8 Design Variables: Iteration 203

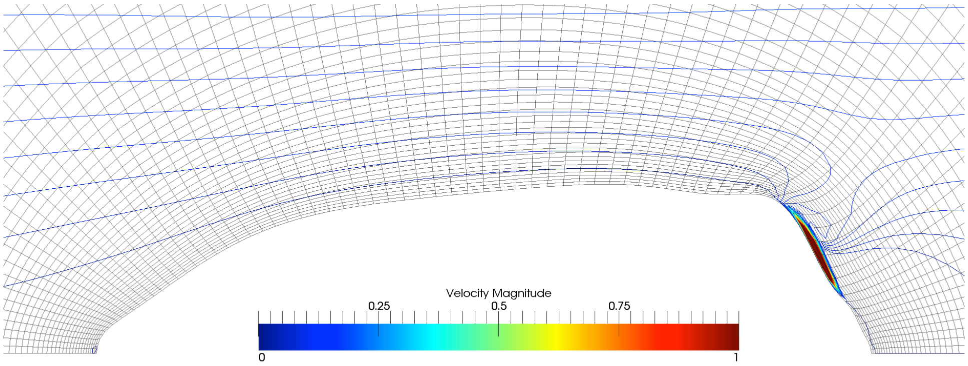

Figure 4.10 Elliptical Shape Design With 8 Design Variables: Iteration 205

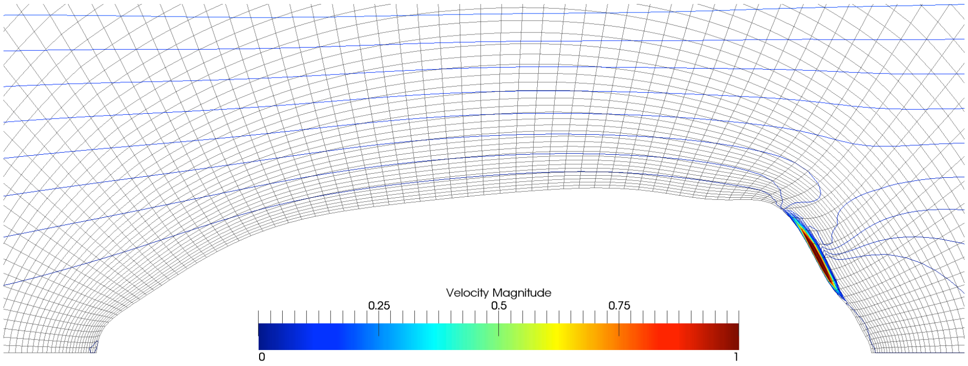

Figure 4.11 Elliptical Shape Design With 8 Design Variables: Iteration 206

Figure 4.12 shows the evaluations of the cost function for each set of valid design variables requested by Dakota and Figure 4.13 shows the corresponding areas for each of the cost evaluations. Although the cost is chatotic at first, Dakota begins to identify a family of configurations which produce a significantly lower cost. Unfortunately, the area constraint of 1.0e-08 is never met and the cost for the more optimized shapes is still in the 1000s, indicating that the strain rate is not $> 100\text{s}^{-1}$ everywhere.

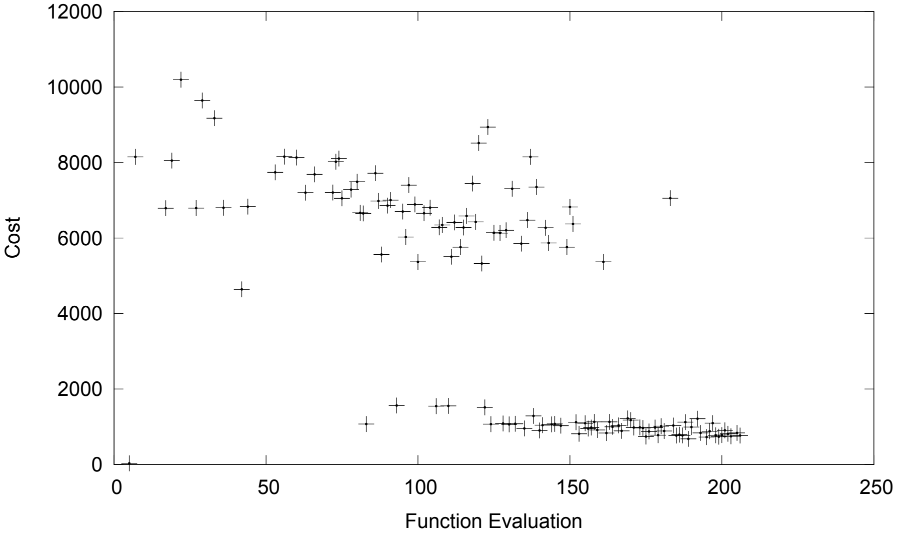

Figure 4.12 Convergence of Design of the Elliptical Stent Using 8 Design Variables

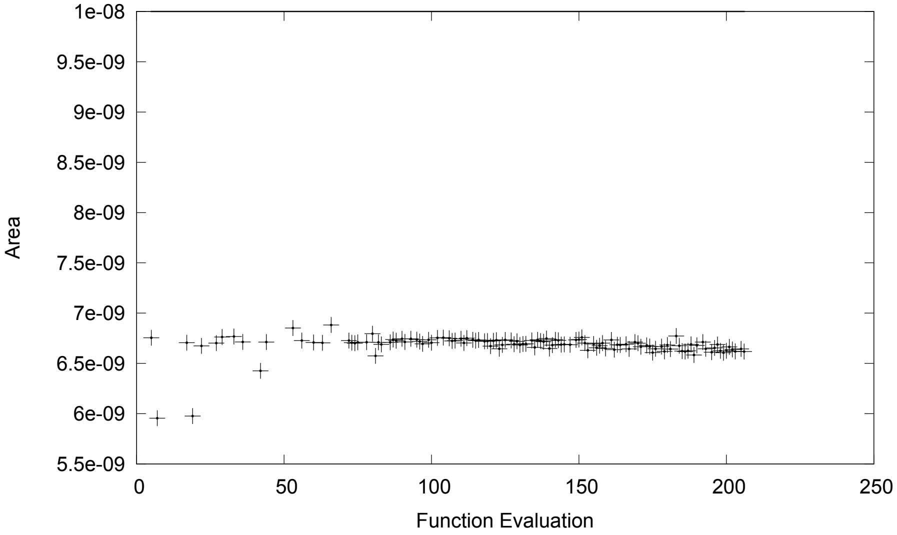

Figure 4.13 Area of Designs of the Elliptical Stent Using 8 Design Variables

12 Design Variables

Figures 4.14 - 4.18 show the first 5 valid meshes produced in the design process using the elliptical starting shape and 12 design variables. Just as with the 8 design variable case, these images show variations on 2 distinct shapes.

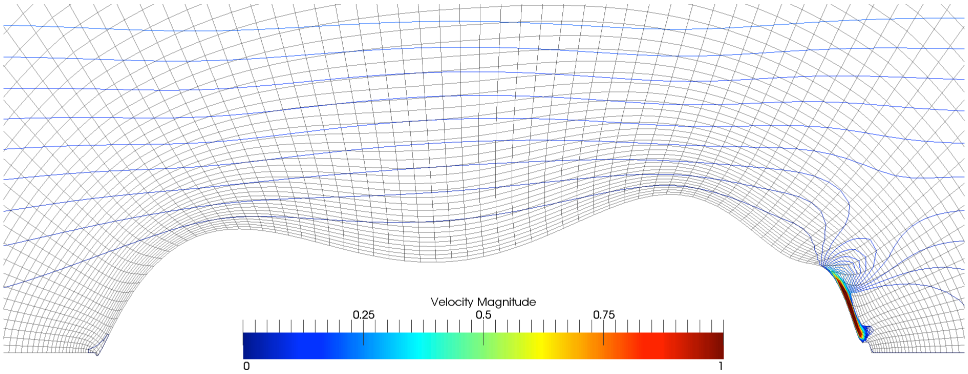

Figure 4.14 Elliptical Shape Design With 12 Design Variables: Iteration 18

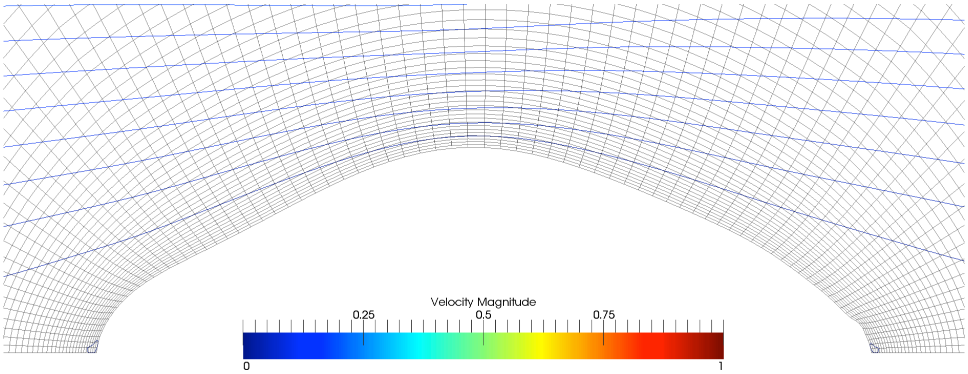

Figure 4.15 Elliptical Shape Design With 12 Design Variables: Iteration 28

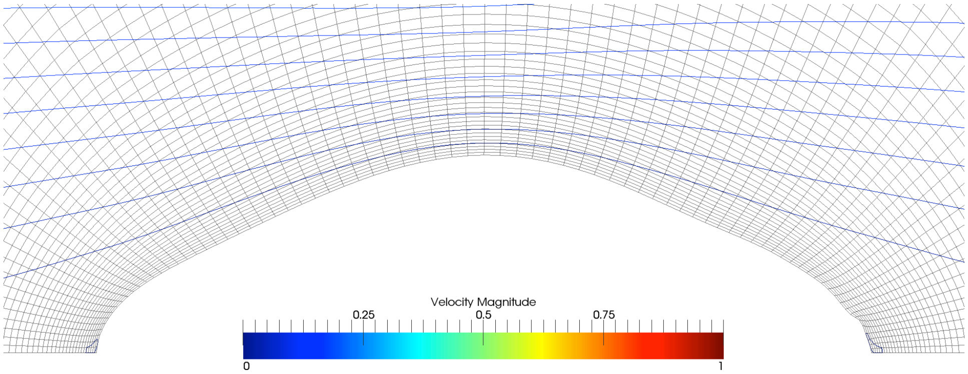

Figure 4.16 Elliptical Shape Design With 12 Design Variables: Iteration 32

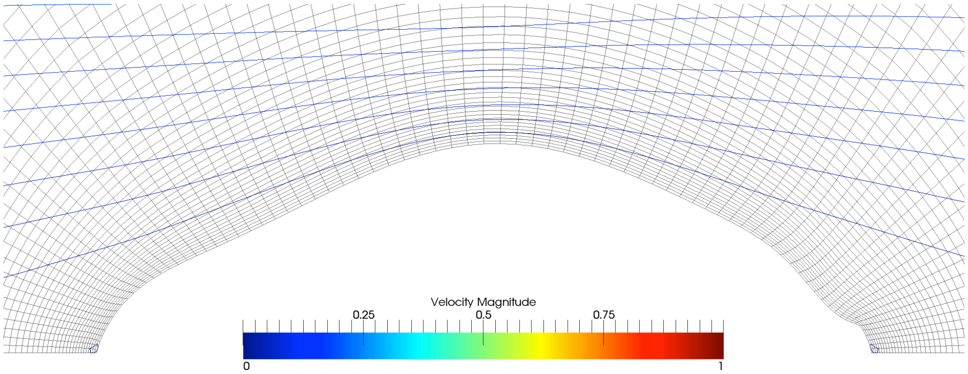

Figure 4.17 Elliptical Shape Design With 12 Design Variables: Iteration 40

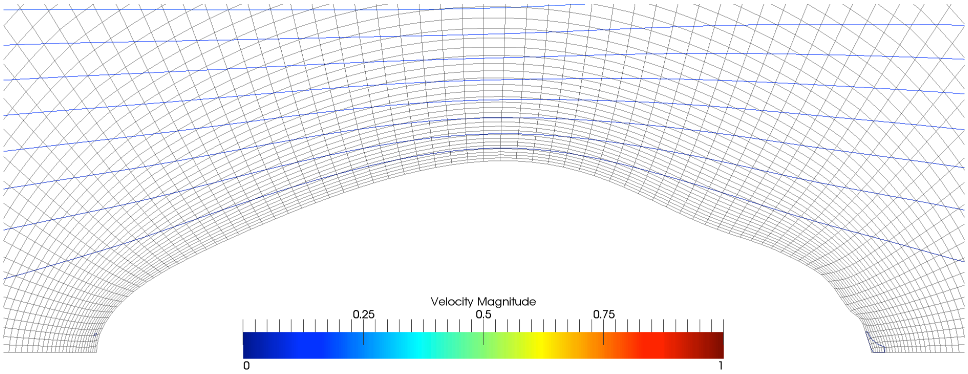

Figure 4.18 Elliptical Shape Design With 12 Design Variables: Iteration 49

Figures 4.19 - 4.21 show the final 3 meshes of the design process. These images indicate that Dakota is designing towards a symmetric shape. This shape is very different from the final shape in the 8 design variable case and does not have a region of high velocity along the back of the stent. Also the recirculation zone behind the stent is smaller than it was in 8 design variable case.

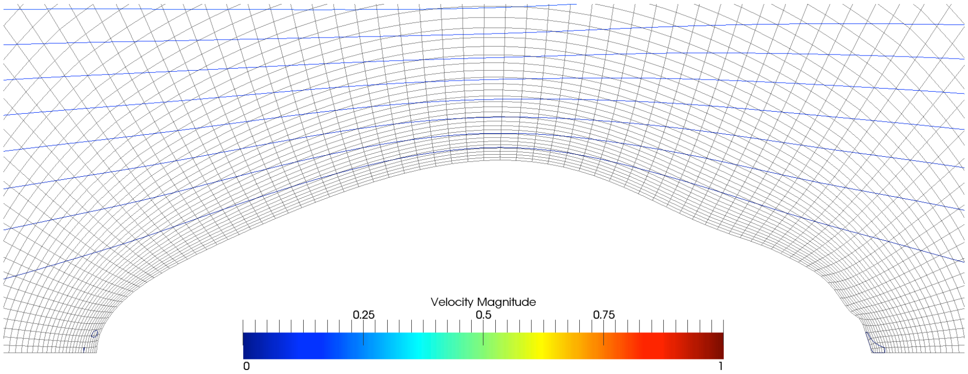

Figure 4.19 Elliptical Shape Design With 12 Design Variables: Iteration 194

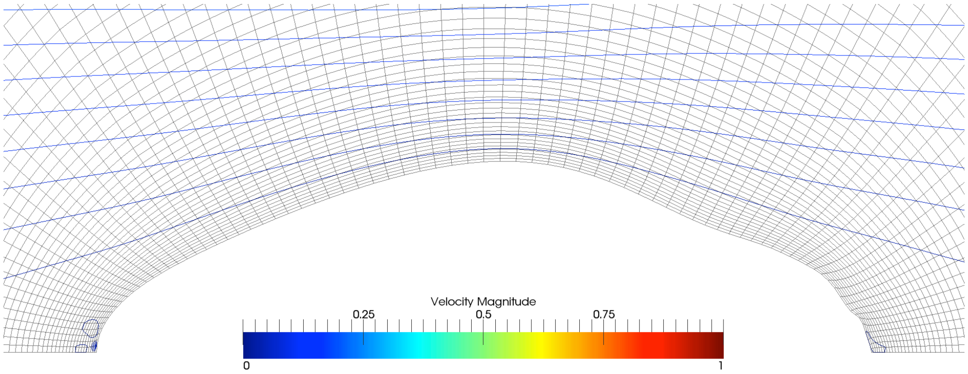

Figure 4.20 Elliptical Shape Design With 12 Design Variables: Iteration 195

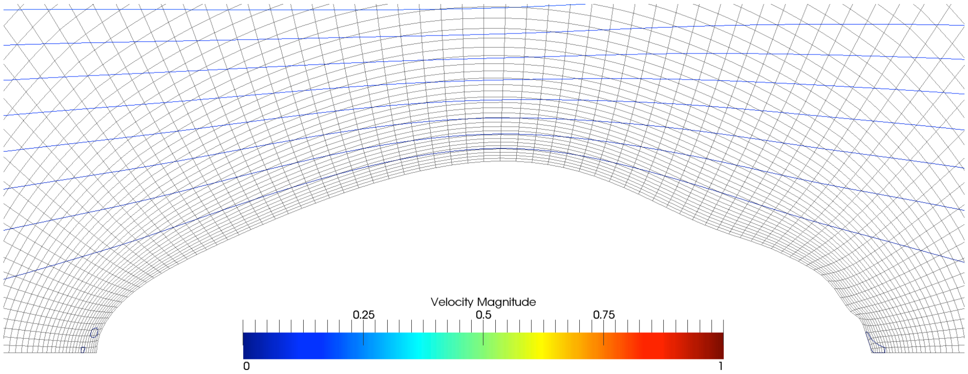

Figure 4.21 Elliptical Shape Design With 12 Design Variables: Iteration 197

Figure 4.22 shows the convergence of the design process using 12 design variables and the initial elliptical shape. The corresponding areas are shown in Figure 4.23. This case was able to more quickly identify a family of optimal configurations, but the cost is still very high. The areas observed are slightly higher than for the case with 8 design variables, but they still do not meet the constraint.

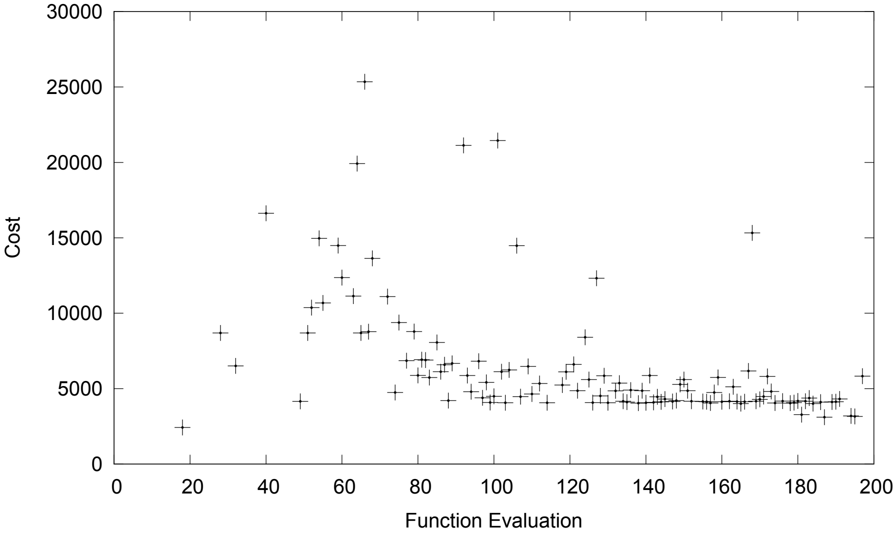

Figure 4.22 Convergence of Design of the Elliptical Stent Using 12 Design Variables

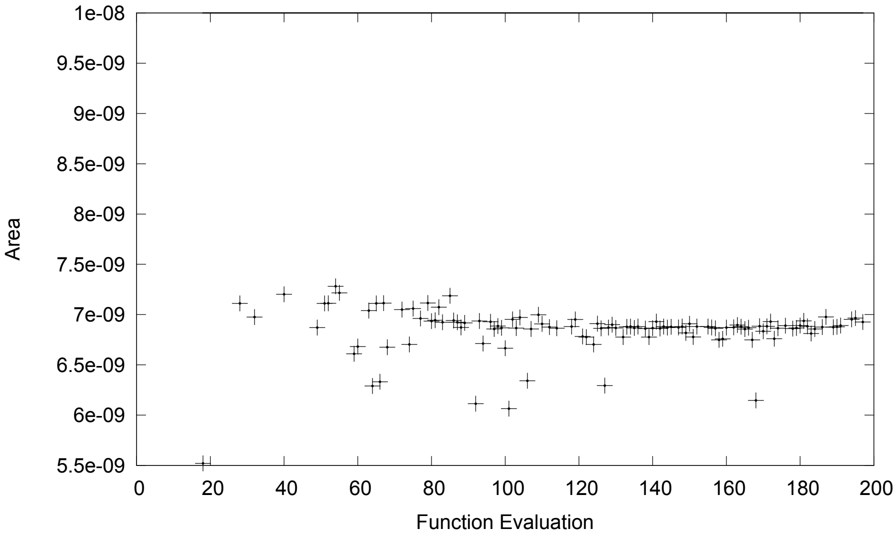

Figure 4.23 Area of the Designs of the Elliptical Stent Using 12 Design Variables

15 Design Variables

Figures 4.24 - 4.28 show the first 5 valid meshes produced in the design process using the elliptical starting shape and 15 design variables. Unlike the case for 8 and 12 design variables, these images show only variations on one distinct shape.

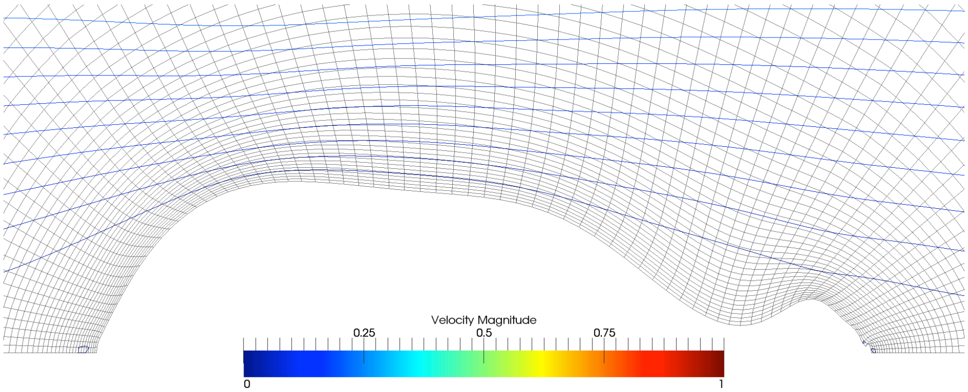

Figure 4.24 Elliptical Shape Design With 15 Design Variables: Iteration 8

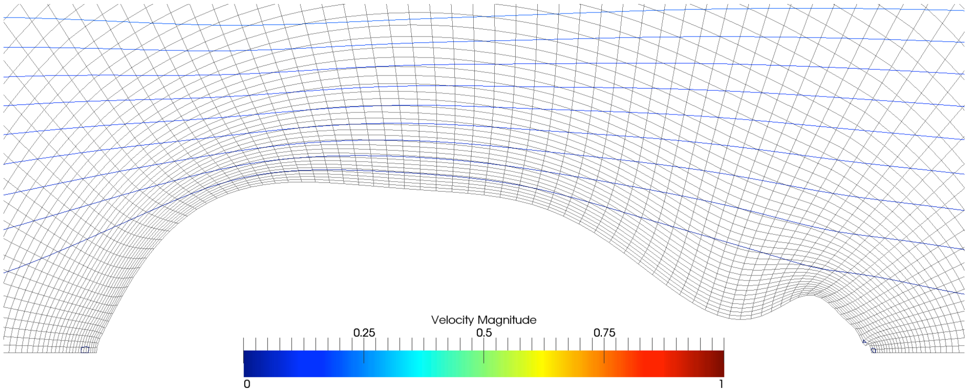

Figure 4.25 Elliptical Shape Design With 15 Design Variables: Iteration 11

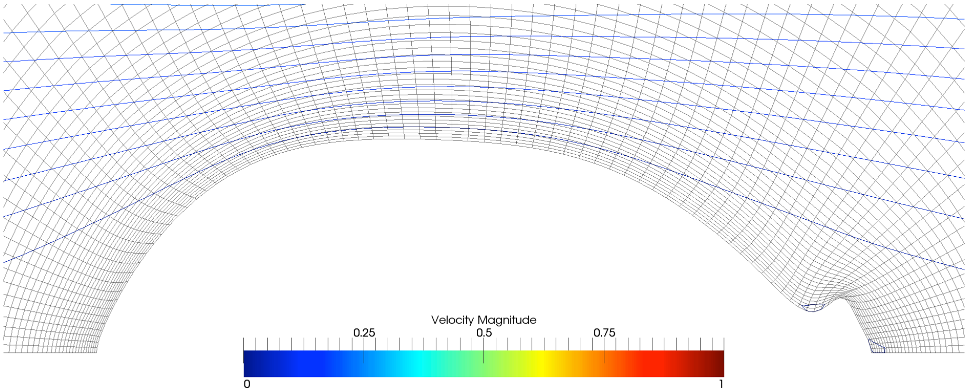

Figure 4.26 Elliptical Shape Design With 15 Design Variables: Iteration 17

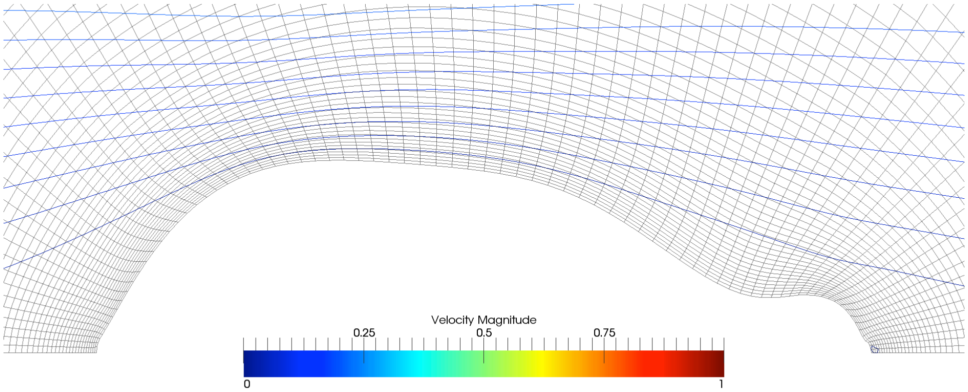

Figure 4.27 Elliptical Shape Design With 15 Design Variables: Iteration 20

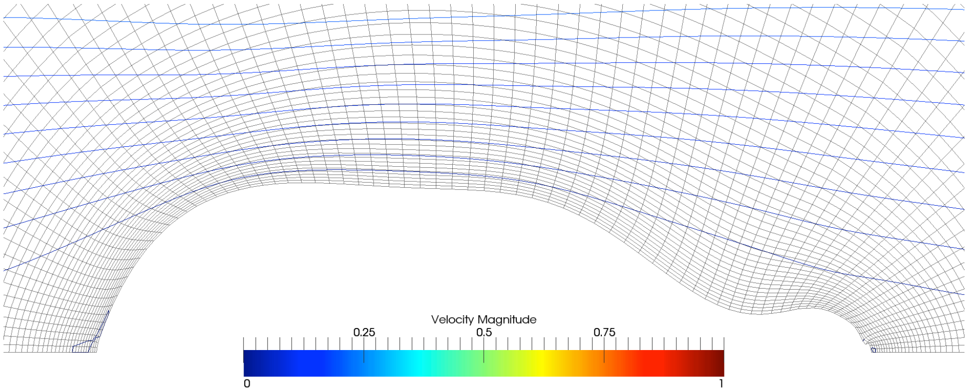

Figure 4.28 Elliptical Shape Design With 15 Design Variables: Iteration 21

Figures 4.29 - 4.31 show the final 3 meshes produced in the design process. Again, the design process converged to a completely different shape than that observed in either the 8 or 12 design variable cases. This shape has a region of high velocity along the back of the stent, just as with the 8 design variable case, and the recirculation zone behind the stent has not been improved.

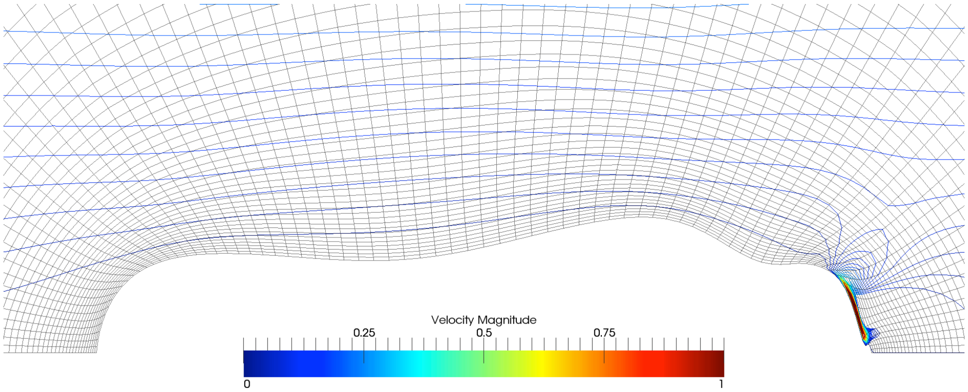

Figure 4.29 Elliptical Shape Design With 15 Design Variables: Iteration 197

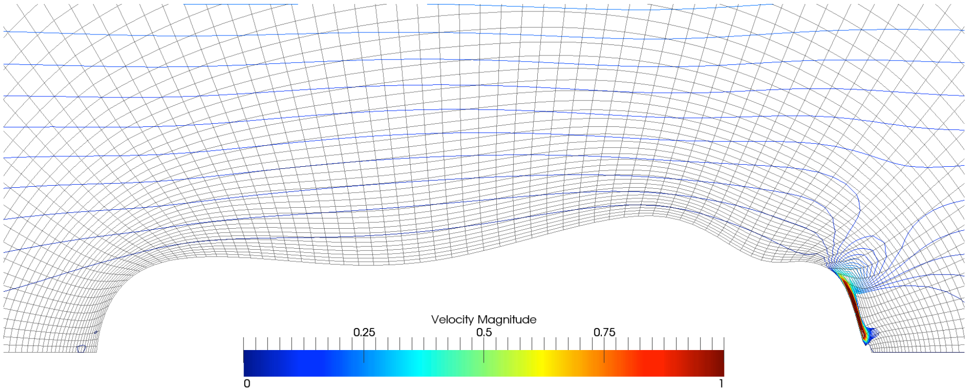

Figure 4.30 Elliptical Shape Design With 15 Design Variables: Iteration 198

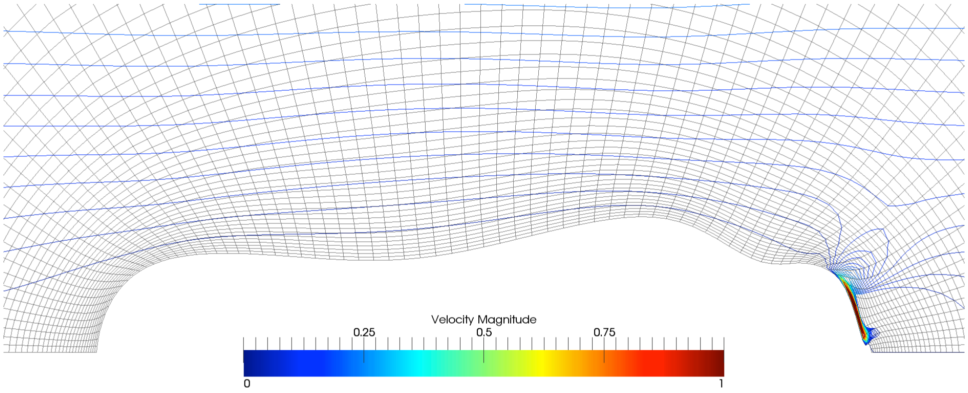

Figure 4.31 Elliptical Shape Design With 15 Design Variables: Iteration 200

Figure 4.32 shows the convergence of the cost for designing the elliptical stent with 15 design variables and the corresponding areas can be seen in Figure 4.33. This case produced significantly lower costs than either the 8 or 12 design variable cases, however the area constraint was still not met.

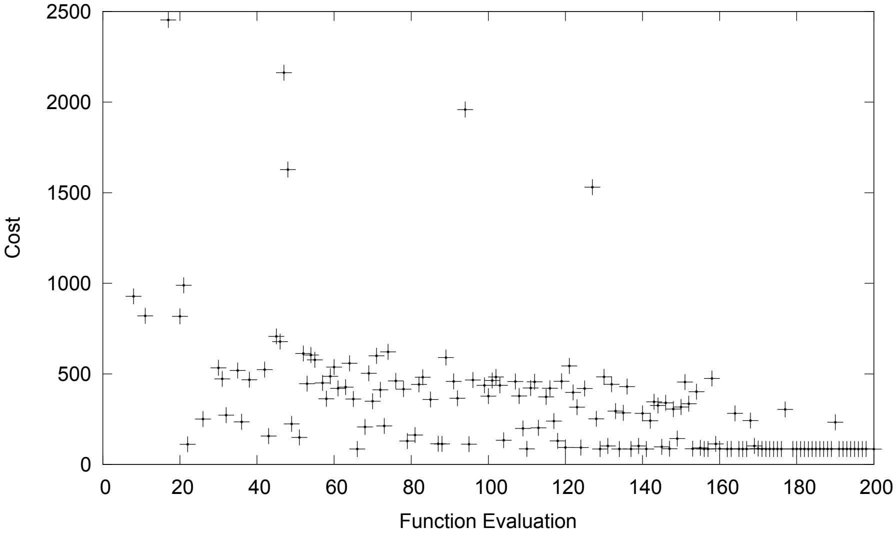

Figure 4.32 Convergence of Design of the Elliptical Stent Using 15 Design Variables

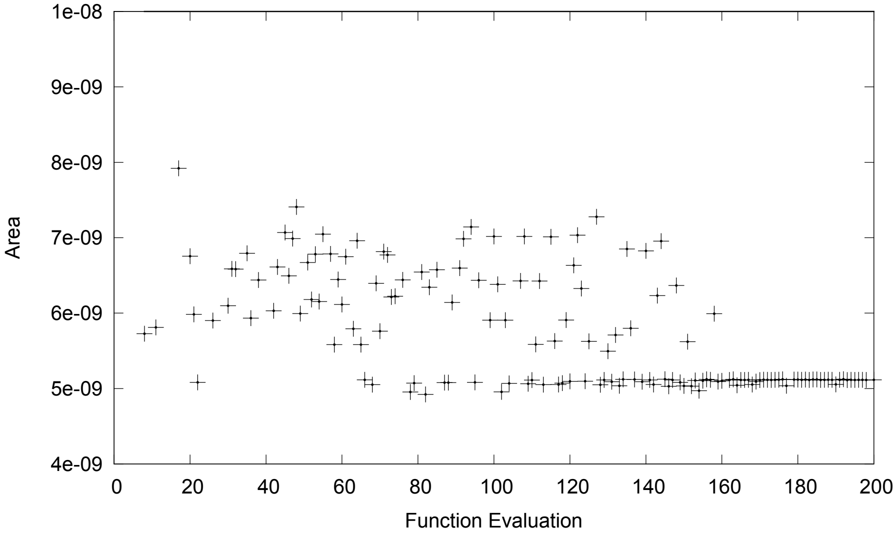

Figure 4.33 Area of Designs of the Elliptical Stent Using 15 Design Variables

Design of the Exponential Shaped Stent

The exponential shape was considered for design since it was proposed as a streamlined stent by Chen *et al.* [17]. This case was performed using 12 design variables. Figures 4.34 - 4.38 show the first 5 valid meshes produced in the design process. Four of these shapes still resemble the initial exponential shape. It is interesting to note that several of these shapes dip below the level of the blood vessel wall towards the back of the stent. In reality, a portion of the stent's thickness sinks into the wall of the blood vessel. Thus, a slight dip below the level of the blood vessel may be producible.

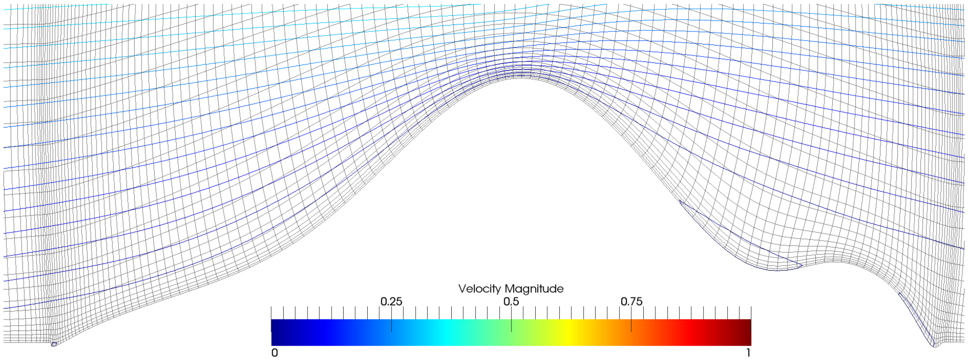

Figure 4.34 Exponential Shape Design With 12 Design Variables: Iteration 2

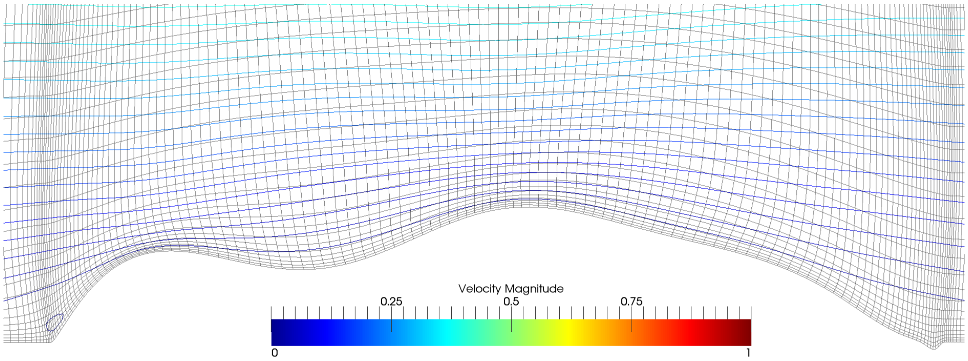

Figure 4.35 Exponential Shape Design With 12 Design Variables: Iteration 3

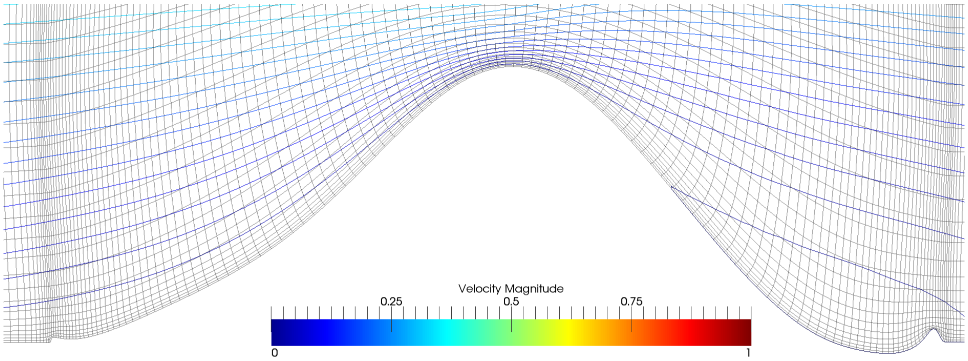

Figure 4.36 Exponential Shape Design With 12 Design Variables: Iteration 7

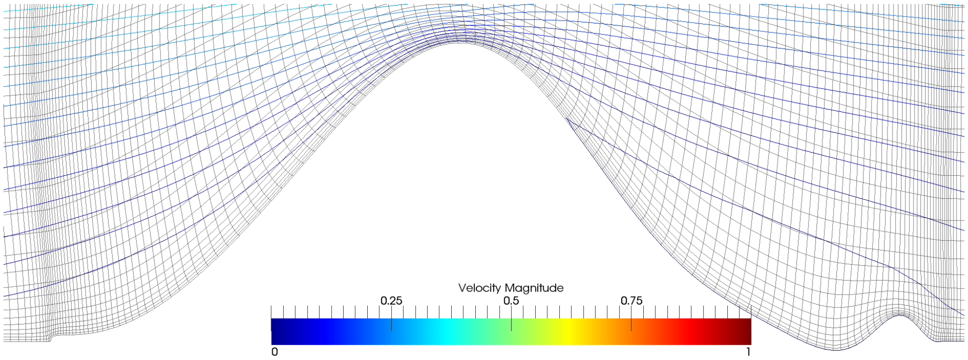

Figure 4.37 Exponential Shape Design With 12 Design Variables: Iteration 8

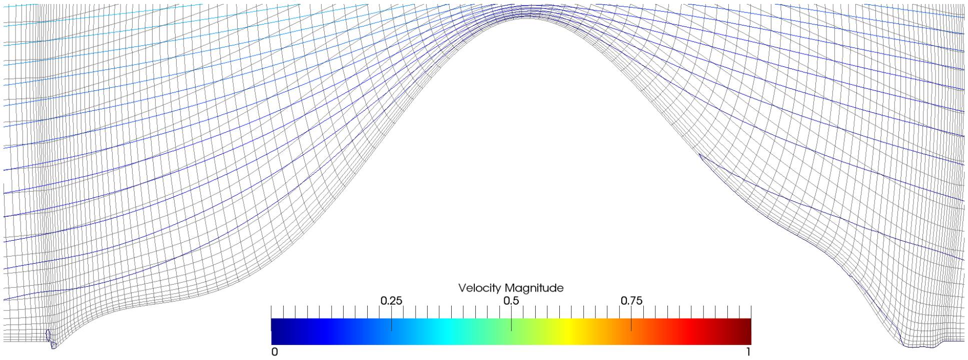

Figure 4.38 Exponential Shape Design With 12 Design Variables: Iteration 9

Figures 4.39 - 4.41 show the final 3 valid meshes produced in the design process. Dakota seems to be designing toward an elliptical-like shape with a lower peak, which has a portion that extends below the level of the blood vessel wall. This shape is very different than any of the shapes obtained using the initial elliptical shape and the recirculation zone behind the stent is nearly eliminated.

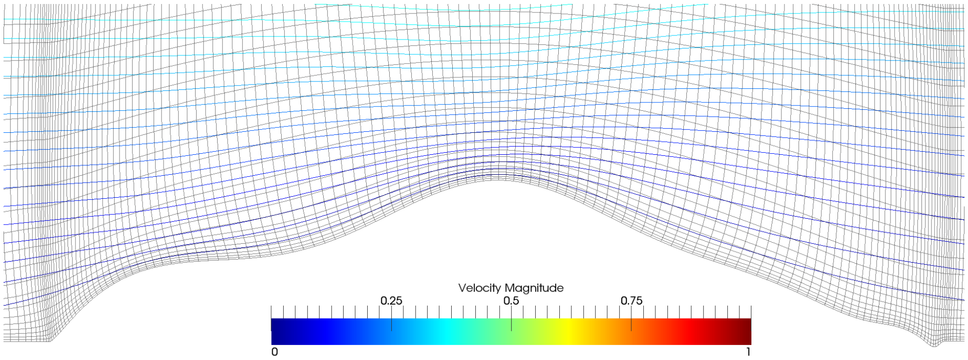

Figure 4.39 Exponential Shape Design With 12 Design Variables: Iteration 126

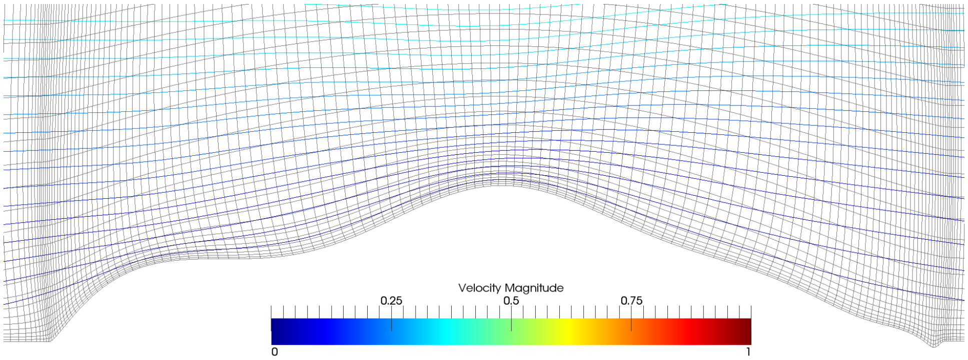

Figure 4.40 Exponential Shape Design With 12 Design Variables: Iteration 127

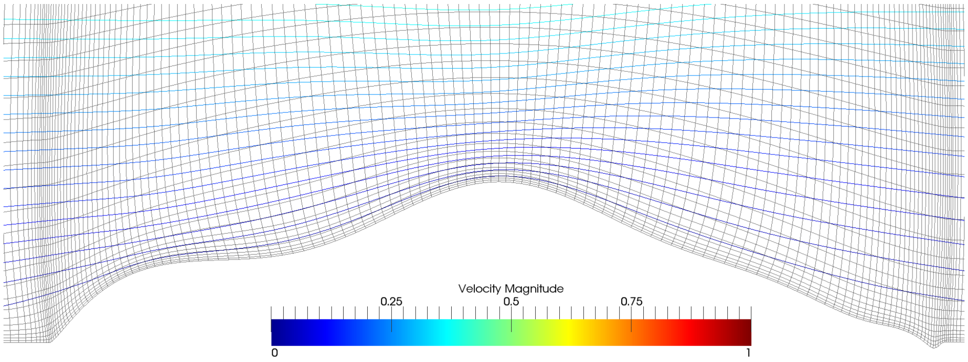

Figure 4.41 Exponential Shape Design With 12 Design Variables: Iteration 128

Figure 4.42 shows the convergence of the cost for the design process and Figure 4.43 shows the corresponding areas. This shape quickly converged to an optimal family of configurations which have very low costs and all of the areas observed satisfied the area constraint, making this a good candidate for an improved stent shape.

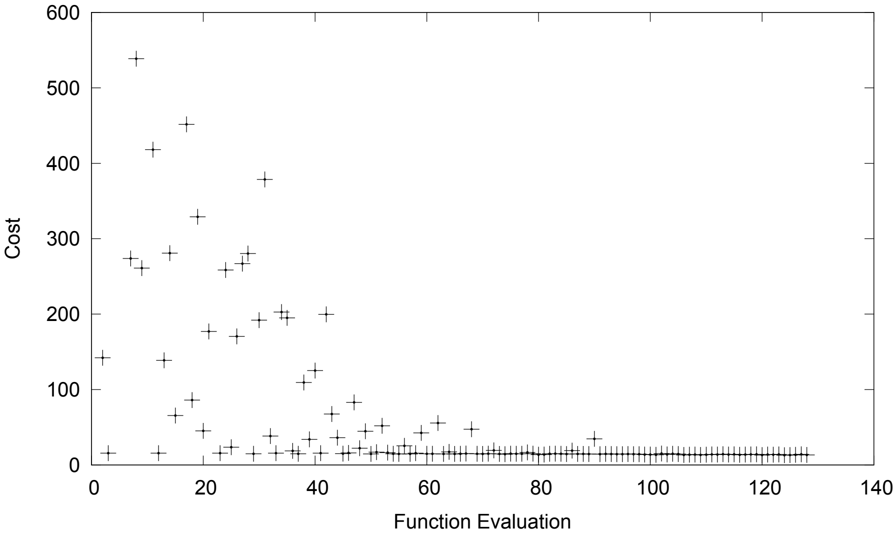

Figure 4.42 Convergence of Design of the Exponential Stent Using 12 Design Variables

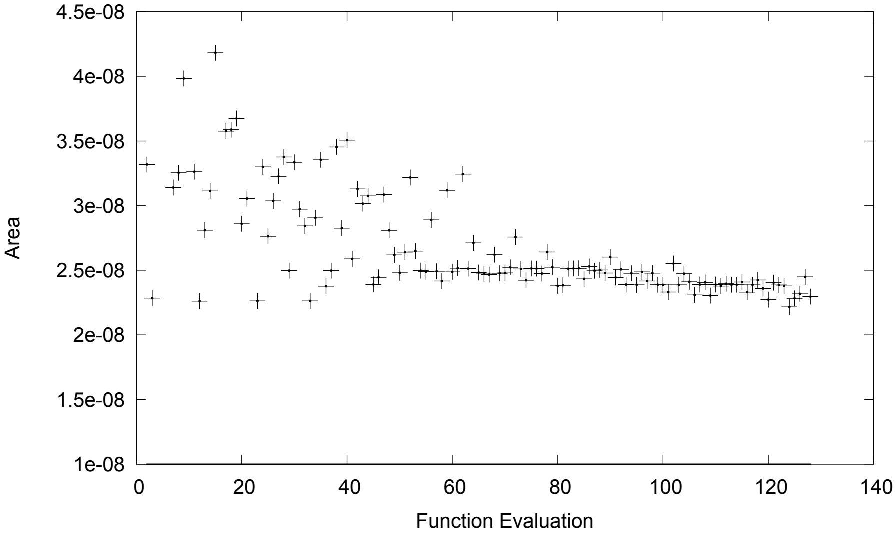

Figure 4.43 Area of Designs of the Exponential Stent Using 12 Design Variables

Design of the Airfoil Shaped Stent

Airfoils are very streamlined and so the shape was considered as a possibility for stent design. Since the Hicks-Henne functions were developed for use with airfoils, only 8 design variables were used for this case. Figures 4.44 - 4.48 show the first 5 valid meshes produced in the design process. All of these shapes are airfoil-like with differences in the height of the peak. They all also have a final dip below the level of the blood vessel wall, similar to the exponential shaped designs. Although the recirculation zone at the front edge of the stent is more pronounced than in other cases, several of these early designs have virtually no recirculation at the back of the stent, which is where most of the problems contributing to restenosis occur.

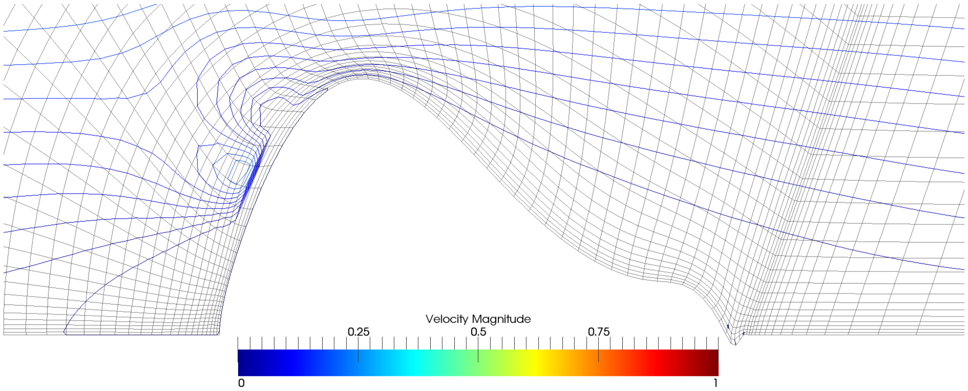

Figure 4.44 Airfoil Shape Design With 8 Design Variables: Iteration 7

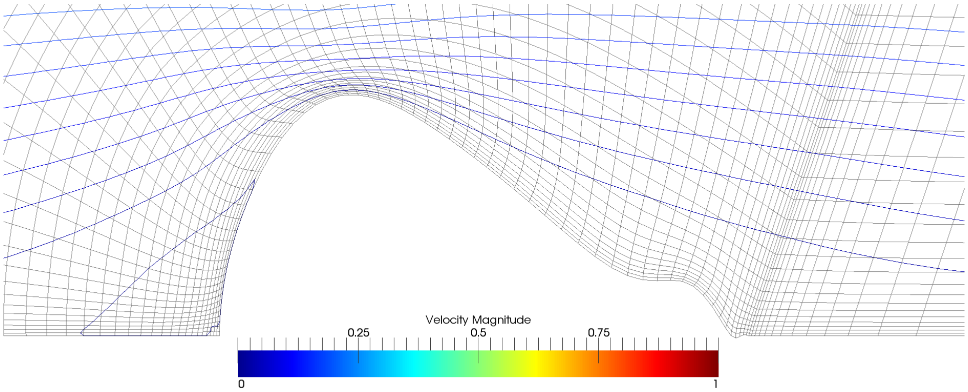

Figure 4.45 Airfoil Shape Design With 8 Design Variables: Iteration 23

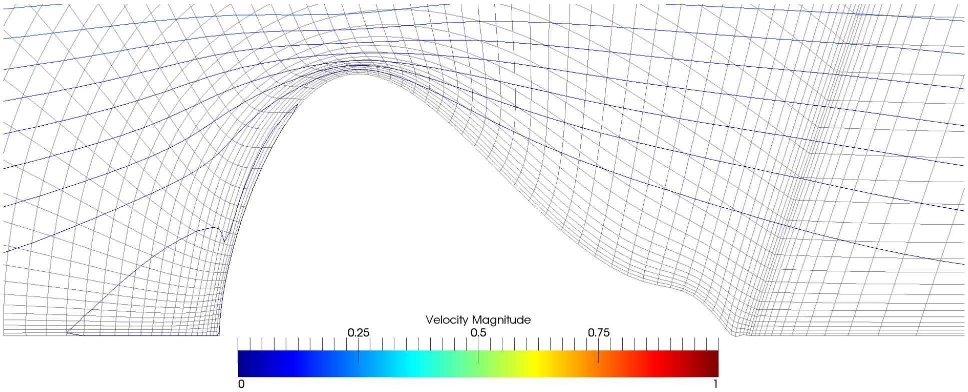

Figure 4.46 Airfoil Shape Design With 8 Design Variables: Iteration 29

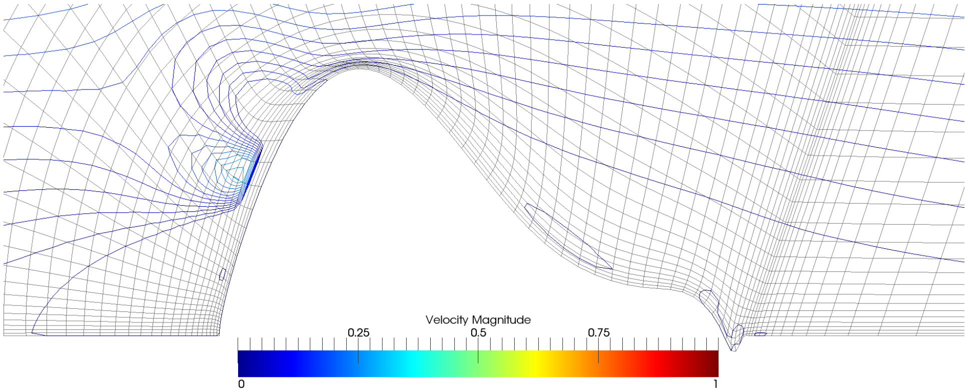

Figure 4.47 Airfoil Shape Design With 8 Design Variables: Iteration 33

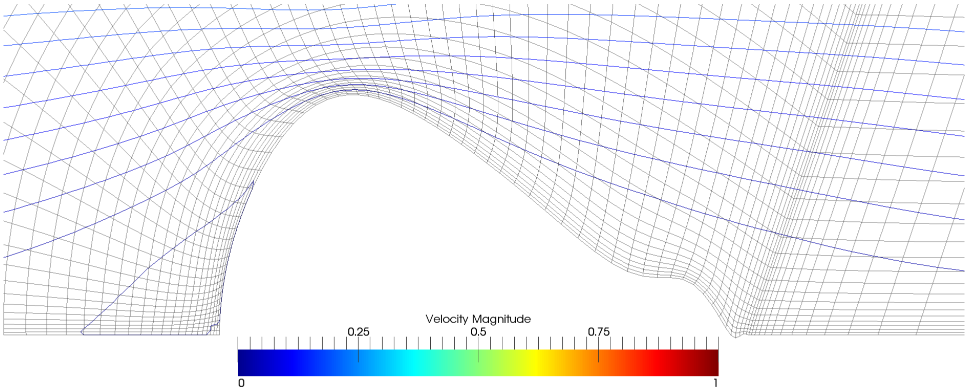

Figure 4.48 Airfoil Shape Design With 8 Design Variables: Iteration 35

Figures 4.49 - 4.51 show the final 3 meshes produced in the design process. These shapes are very similar to one another. These later designs do not dip below the level of the blood vessel wall, indicating the Dakota is designing away from that option. This shape has a region of very high velocity along the front of the stent and also a very large recirculation zone at the front. Unfortunately the mesh is inverted at the leading edge of the stent, indicating that there needs to be improved analysis of mesh quality in the code.

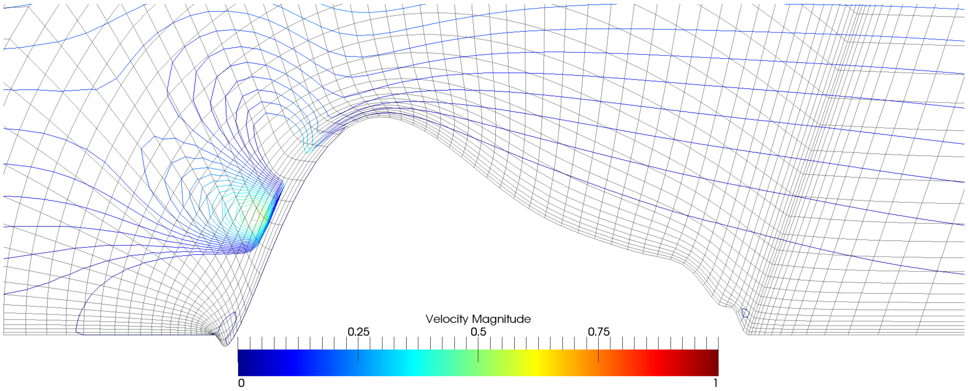

Figure 4.49 Airfoil Shape Design With 8 Design Variables: Iteration 218

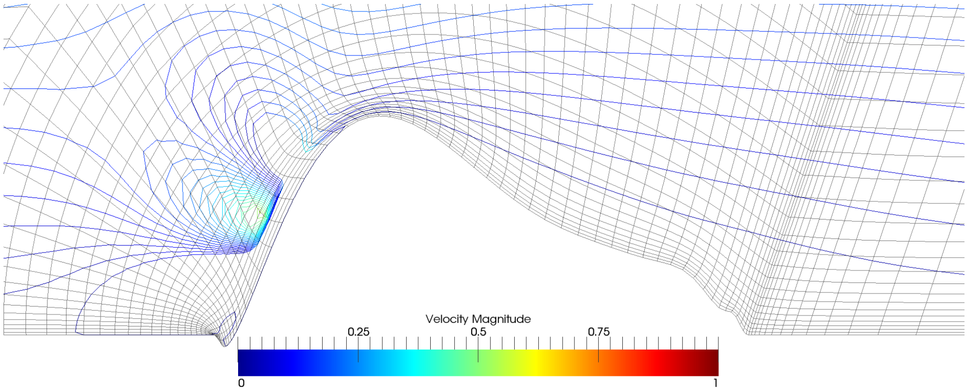

Figure 4.50 Airfoil Shape Design With 8 Design Variables: Iteration 219

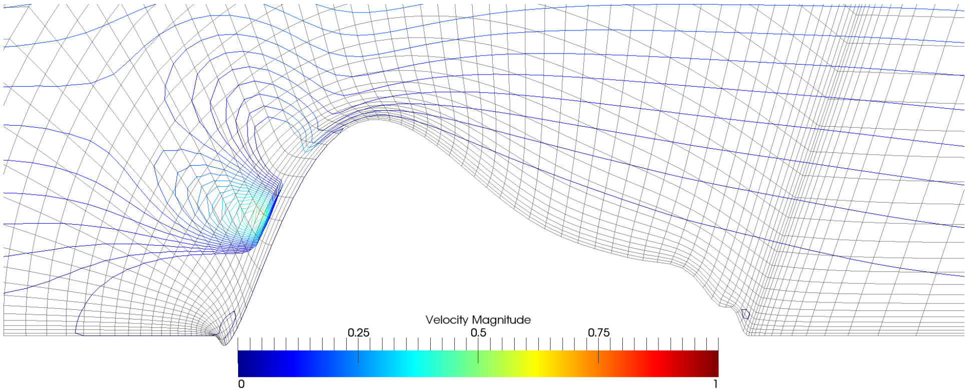

Figure 4.51 Airfoil Shape Design With 8 Design Variables: Iteration 220

Figure 4.52 shows the convergence of the design process. As with the exponential shape, the naturally streamlined initial shape of the airfoil also produced lower values of cost. Figure 4.53 shows the areas corresponding to each of the cost function evaluations. In the figure a reference line has been drawn to indicate the area constraint. Although there was a decreasing trend for the areas observed, many were above the threshold. If further constraints were placed on the shape to ensure the mesh would not be inverted, this case may produce results which meet the area constraint. However, unless the recirculation zone at the leading edge of the stent is greatly reduced, this cannot be considered a good candidate for an improved stent shape.

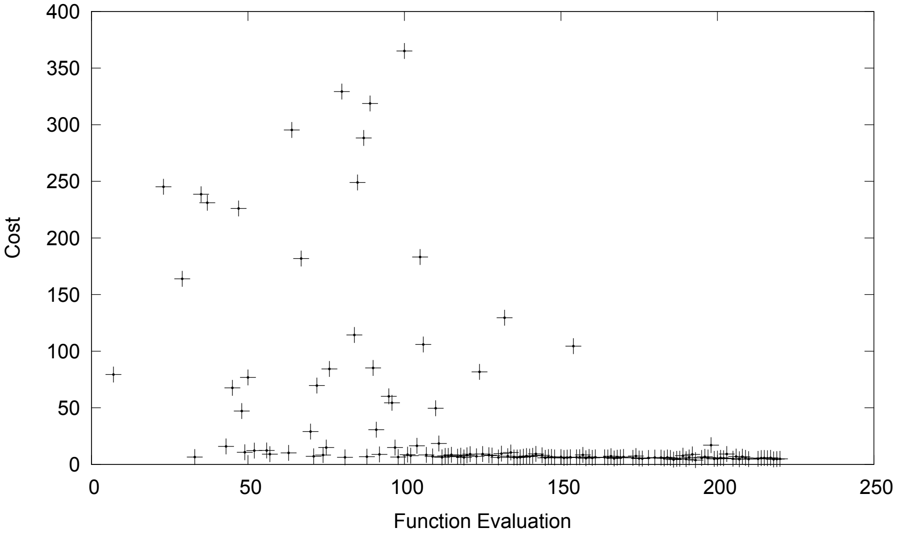

Figure 4.52 Convergence of Design of the Airfoil Stent Using 8 Design Variables

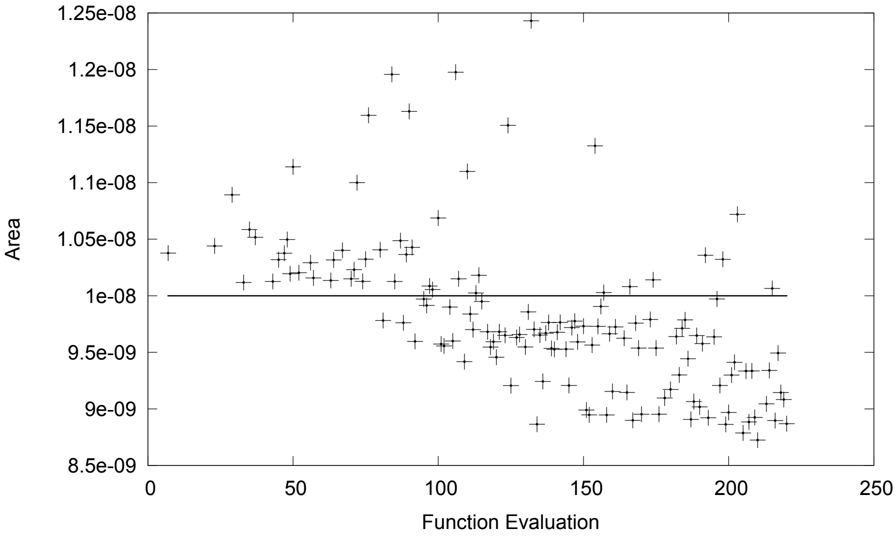

Figure 4.53 Area of Designs of the Airfoil Stent Using 8 Design Variables

Design of the Stent Starting from a Flat Curve

The ideal scenario for improving shear rate and shear stress is to have no stent in the blood vessel, which is usually not the case after PCI treatment. It was decided to use the true ideal scenario as a starting place for design to see if the random initial population of the evolutionary algorithm and the area constraint would be enough to find a valid option which improves the stent design. Figures 4.54 - 4.58 show the first 5 valid meshes produced in the design process. These images identify two different design options, one that is symmetric and curved and another that is a plateau shape with a slight dip in the center.

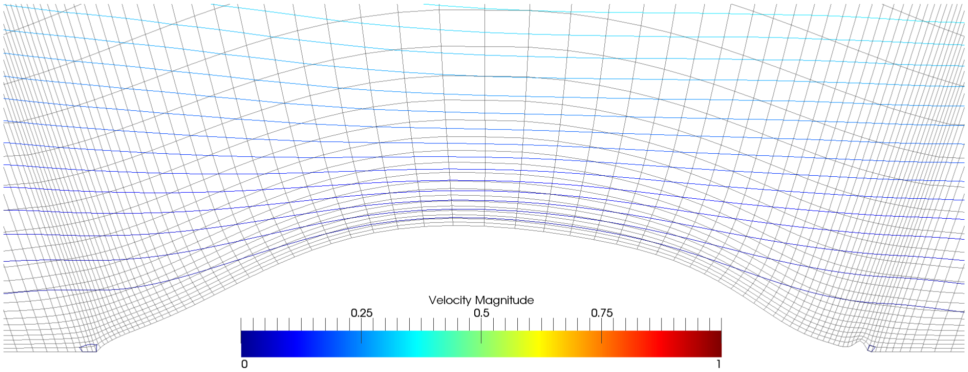

Figure 4.54 Stent Design Starting from a Flat Plate With 8 Design Variables: Iteration 1

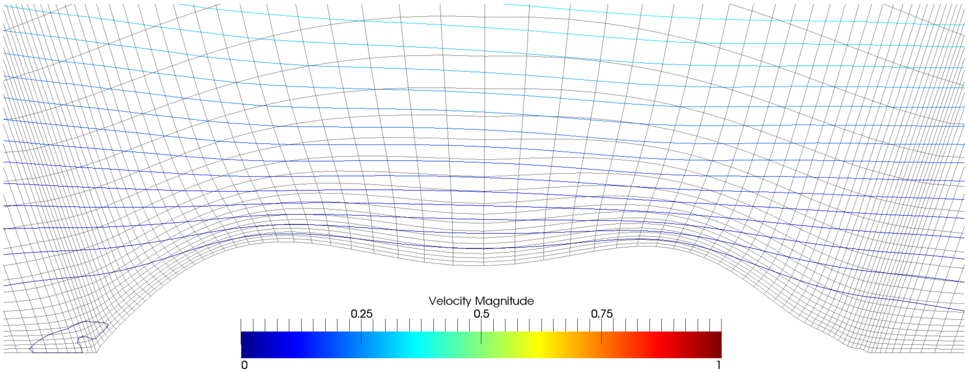

Figure 4.55 Stent Design Starting from a Flat Plate With 8 Design Variables: Iteration 2

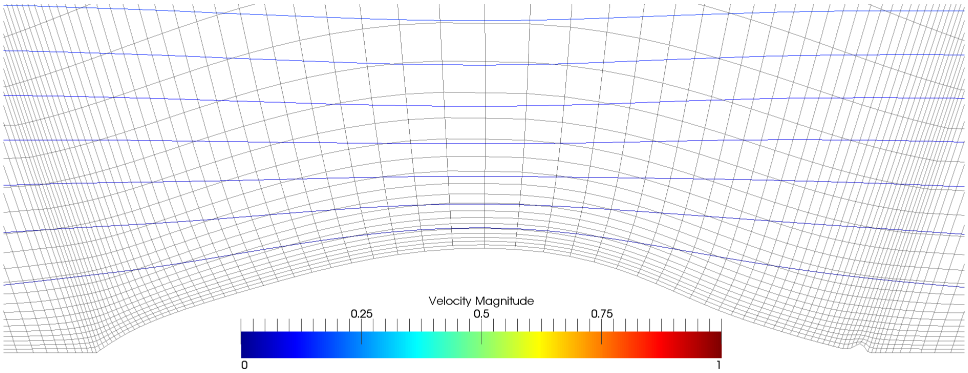

Figure 4.56 Stent Design Starting from a Flat Plate With 8 Design Variables: Iteration 7

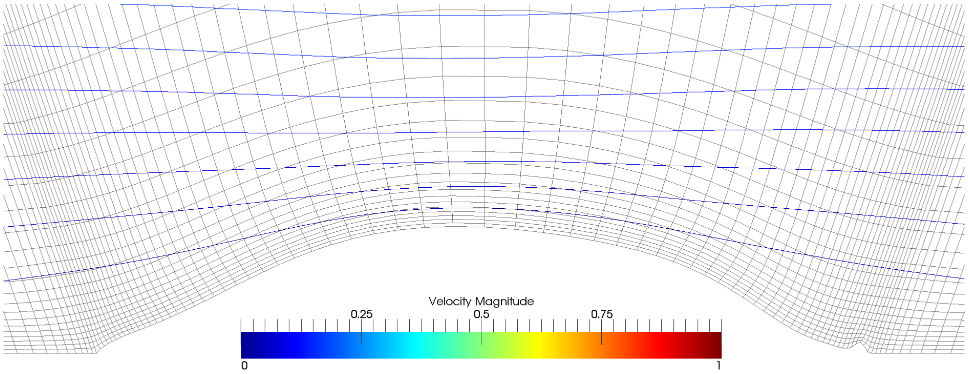

Figure 4.57 Stent Design Starting from a Flat Plate With 8 Design Variables: Iteration 11

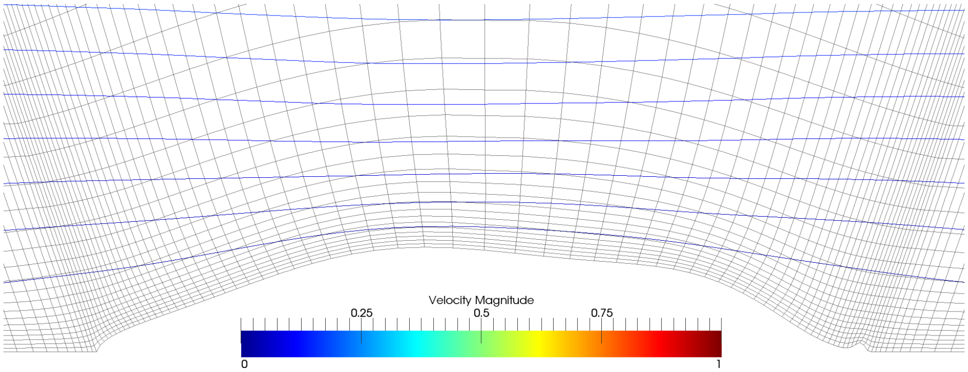

Figure 4.58 Stent Design Starting from a Flat Plate With 8 Design Variables: Iteration 15

Figures 4.59 - 4.61 show the final 3 meshes produced in the design process. This case converged to a somewhat symmetric shape with very little recirculation in either the front or the back of the stent. This shape is most similar to that produced using the exponential initial mesh, but the height of the stent is much lower. This shape also has a slight bump at the trailing edge of the stent. This is likely a remnant of the evolutionary process rather than an optimized design since the stent would still have very little recirculation without it.

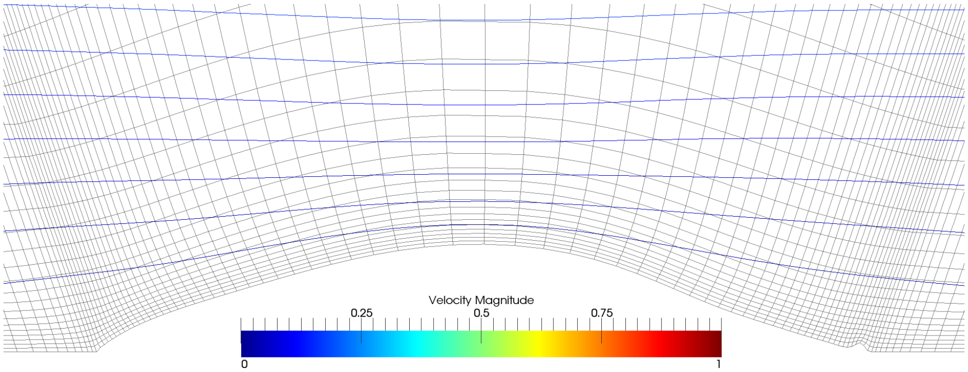

Figure 4.59 Stent Design Starting from a Flat Plate With 8 Design Variables: Iteration 143

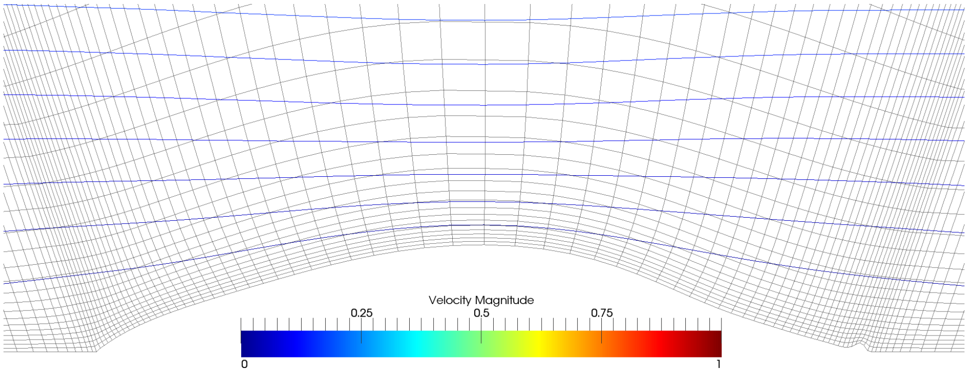

Figure 4.60 Stent Design Starting from a Flat Plate With 8 Design Variables: Iteration 144

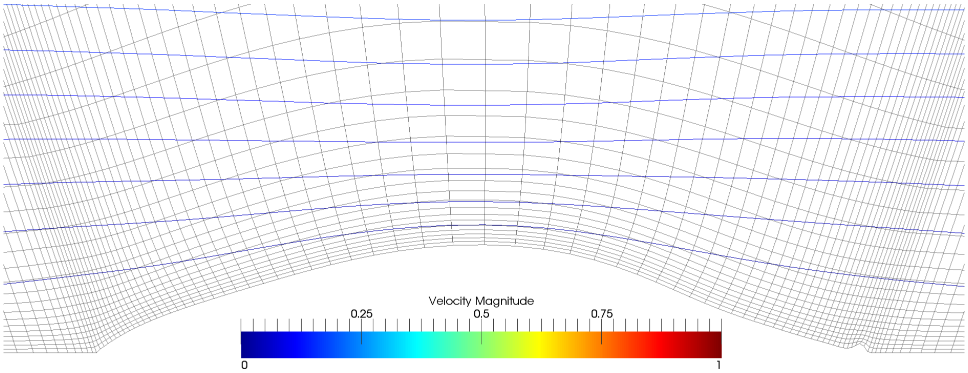

Figure 4.61 Stent Design Starting from a Flat Plate With 8 Design Variables: Iteration 146

Figure 4.62 shows the convergence of the designing using 12 design variables and a flat starting position and Figure 4.63 shows the corresponding areas. The cost in general is very low, with many around or below a value of 10, however this case produced the smallest areas thus far observed. Therefore improvements need to be made in the constraints used to ensure proper area or height for the stent.

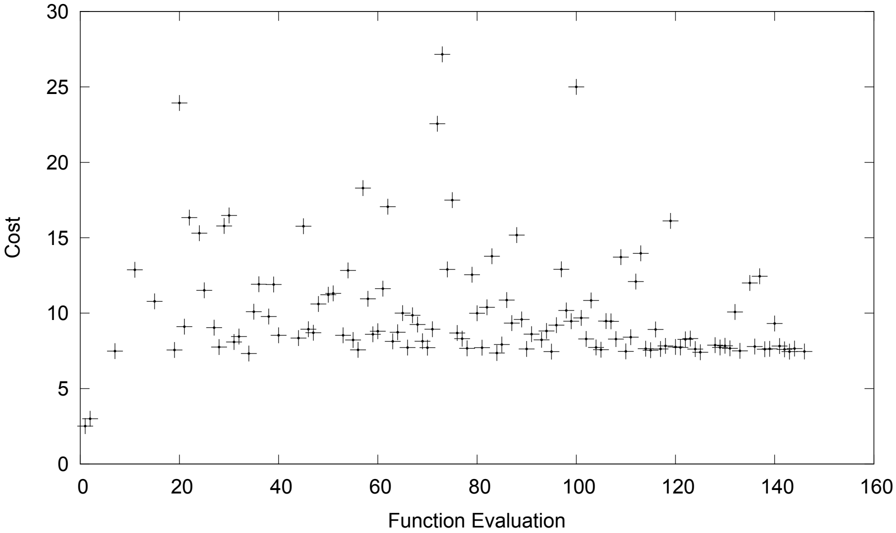

Figure 4.62 Convergence of Stent Design Starting from a Flat Plate Using 12 Design Variables

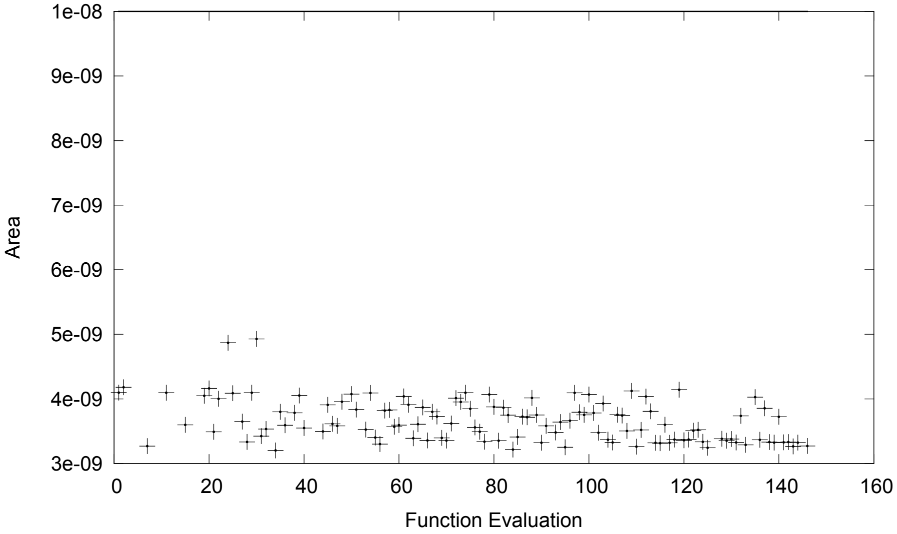

Figure 4.63 Area of Stent Designs Starting from a Flat Plate Using 12 Design Variables

CHAPTER 5

CONCLUSIONS

The goal of this work was to implement a two-dimensional, compressible flow solver that is capable of simulating blood flow through stented arteries and then to interface the flow solver and a mesh movement routine with Dakota to improve arterial stent design. The ability to simulate blood flow was verified by comparing the results to analytic solutions of the Blasius equation and Couette flow and by comparing results of simulations through stented arteries to results found in other studies. The flow solver was linked with linear elastic mesh movement and an interface was created with Dakota.

Candidate stent designs were found by Dakota using initial meshes with elliptical, exponential, airfoil, and flat shaped stent sections. All of the resulting candidate stent shapes differed greatly from one another, indicating that the results are highly dependent on the initial shape used for the design process. Regardless of the number of design variables used, the elliptical shape failed to produce low costs and never met area constraint. The exponential shape produced results with low costs, areas above the constraint, and reduced recirculation zones. The airfoil shape nearly met the area costraint and also had low costs, but the recirculation zone at the leading edge was more pronounced and the final meshes were inverted at the leading edge. The flat shape produced the lowest costs overall, but failed to meet the area constraint. Thus the only the exponential shape can be considered a good candidate for improving stent design.

Improvements can be made to the design process in several areas. The flow solver will more accurately simulate blood flow when incompressibility, the extension to three dimensions, and the ability to model pulsatile flow are added. The computational time could be reduced by adding parallelism and the ability to compute derivatives needed for gradient-based optimization methods. The results obtained here would provide a good starting place for gradient-based methods. Furthermore, since the designs obtained using Hicks-Henne functions are dependent upon the initial mesh and there are some issues with smoothness using this parametrization, other forms of parametrization should be considered which do not have this dependency and better satisfy smoothness requirements. Finally, the recirculation zones were not entirely eliminated, especially in the airfoil case, indicating that the cost function needs improvment. This is due to the fact that although the flow is in the wrong direction, the shear rate is still relatively high in most of the recirculation zone and is only low at the reattachment point. Incorporating a directional component into the cost function would allow the design process to directly minimize the recirculation zones as well as maximizing shear rate.

REFERENCES

[1] Wilmer W Nichols, Michael F O'Rourke, and Charalambos Vlachopoulos. *McDonald's Blood Flow in Arteries: Theoretical, Experimental and Clinical Principles.* Hodder Arnold, 6th edition, 2011. 1, 8, 9

[2] Charles A. Taylor and Mary T. Draney. Experimental and computational methods in cardiovascular fluid mechanics. *Annu. Rev. Fluid Mech.*, 36:197–231, 2004. 1, 5

[3] J. Wouter Jukema, Tarek A. N. Ahmed, Jeffrey J. W. Verschuren, and Paul H. A. Quax. Restenosis after pci. part 2: prevention and therapy. *Nature Reviews Cardiology*, 9:79–90, 2012. 1, 2

[4] Konstantinos C. Koskinas, Yiannis S. Chatzizisis, Antonios P. Antoniadis, and George D. Giannoglou. Design endothelial shear stress in stent restenosis and thrombosis: Pathophysiologic mechanisms and implications for clinical translation. *Journal of the American College of Cardiology*, 59(15):1337–1349, 2012. 1, 2, 3, 4, 5

[5] J. Wouter Jukema, Jeffrey J. W. Verschuren, Tarek A. N. Ahmed, and Paul H. A. Quax. Restenosis after pci. part 1: pathophysiology and risk factors. *Nature Reviews Cardiology*, 9:53–62, 2012. 2

[6] Juan M. Jimenez and Peter F. Davies. Hemodynamically driven stent strut design. *Ann Biomed Eng.*, 37(8):1483–1494, 2009. 2, 3, 4, 5

[7] Demosthenes Katritsis, Lambros Kaiktisis, Andreas Chaniotis, John Pantos, Efstathios P. Efstathopoulos, and Vasilios Marmarelis. Wall shear stress: Theoretical considerations and methods of measurement. *Progress in Cardiovascular Diseases*, 49(5):307–329, 2007. 5, 6, 7, 8, 9

[8] Brian M. Adams, Lara E. Bauman, William J. Bohnhoff, Keith R. Dalbey, John P. Eddy, Mohamed S. Ebeida, Michael S. Eldred, Patricia D. Hough, Kenneth T. Hu, John D. Jakeman, Laura P. Swiler, and Dena M. Vigil. Dakota reference manual, February 2013. 10, 13

[9] Brian M. Adams, Keith R. Dalbey, Michael S. Edlred, David M. Gay, Laura P. Swiler, William J. Bohnhoff, John P. Eddy, Karen Haskell, Patricia D. Hough, and Sophia Lefantzi. *DAKOTA, A Multilevel Parallel Object-Oriented Framework for Design Optimization, Parameter Estimation, Uncertainty Quantification, and Sensitivity Analysis*. Sandia National Laboratories, 5.1 edition, December 2009. 13

[10] John C. Tannehill, Dale A. Anderson, and Richard H. Pletcher. *Computational Fluid Mechanics and Heat Transfer*. Taylor & Francis, 2nd edition, 1997. 16, 17, 20

[11] W. Kyle Anderson, James L. Thomas, and Bram Van Leer. Comparison of finite volume flux vector splittings for the euler equations. *AIAA Journal*, 24:1453–1460, 1986. 21

[12] D.L. Whitfield and J.M. Janus. Three-dimensional unsteady euler equations solution using flux vector spliting. In *AIAA 17th Fluid Dynamics, Plasma Dynamics, and Lasers Conference*, 1984. 22

[13] Hsiao-Yuan Wu, Shuchi Yang, and Feng Liu. Comparison of three geometric representations of airfoils for aerodynamic optimization. *AIAA Journal*, 2003. 25

[14] Steve L. Karman. Unstructured viscous layer insertion using linear-elastic smoothing. *AIAA Journal*, 45:168–180, 2007. 26, 27

[15] Hermann Schlichting. *Boundary-Layer Theory*. McGraw-Hill Series in Mechaniccal Engineering. McGraw-Hill Book Company, 7th edition, 1979. 28, 29

[16] I. G. Currie. *Fundamental Mechanics of Fluids*. McGraw-Hill, 1974. 30

[17] Zengsheng Chen, Yubo Fan, Xiaoyan Deng, and Zaipin Xu. A new way to reduce flow disturbance in endovasular stents: A numerical study. *Artificial Organs*, 35(4):392–397, 2011. 34, 54

APPENDIX A

DAKOTA INPUT FILE

Below is an example of the Dakota input file used in this study. Although this study only used the evolutionary algorithm, identified as ‘EA’, this input file is also set up to handle the OPT++ quasi-Newton method, identified as method ‘NLP’. Each method requires a model which identifies the appropriate variables, interface, and responses. If Dakota is to use an outside source for the function evaluations, this information needs to be specified in the interface section. Every time a function evaluation is required, Dakota will print the request in the parameters_file specified, call the specified analysis_driver, and wait for the driver to return the specified results_file. The responses section identifies the number of cost functions and any constraints. It may be advantageous to use a combination of methods to solve the problem. For instance, Dakota could use evolutionary algorithm to find an interval which contains the solution and then switch to the Newton method to quickly find that solution. Although not shown here, this can all be specified in the strategy section of the input file.

```
#  DAKOTA INPUT FILE
strategy,
    hybrid sequential
    method_list = ‘EA’
    #graphics
    tabular_graphics_data

method,
    id_method = ‘EA’
    model_pointer = ‘M1’
    max_iterations = 30
    coliny_ea
    seed = 101
    population_size = 10
    crossover_rate = 1.0
    crossover_type = blend
    mutation_type = offset_normal
    mutation_scale = 0.0001
    replacement_type chc = 3
    final_solution = 1
  output debug

method,
```

```
    id_method = ‘NLP’
    model_pointer = ‘M2’
  optpp_q_newton
  max_iterations = 100
    convergence_tolerance = 1e-8
    #max_step = 10.0
    search_method value_based_line_search
  output debug

model,
    id_model = ‘M1’
    single
        variables_pointer = ‘V1’
        interface_pointer = ‘I1’
        responses_pointer = ‘R1’

model,
    id_model = ‘M2’
    single
        variables_pointer = ‘V1’
        interface_pointer = ‘I1’
        responses_pointer = ‘R2’


variables,
    id_variables = ‘V1’
  continuous_design = 15
      cdv_initial_point      0.00  0.1  -0.1   0.00  0.00  0.00  0.00  0.00
      cdv_lower_bounds      -0.02 -0.02 -0.05 -0.05 -0.05 -0.05 -0.05 -0.05
      cdv_upper_bounds       0.02  0.05  0.10  0.10  0.10  0.10  0.10  0.10
      cdv_descriptor         ’h0’  ’h1’  ’h2’  ’h3’  ’h4’  ’h5’  ’h6’  ’h7’
interface,
    id_interface = ‘I1’
    system
    #asynchronous
  analysis_driver = ‘driver_script.py’
    parameters_file = ‘params.in’
    results_file    = ‘results.out’
    #aprepro
    #deactivate active_set_vector
    file_tag      # tag files with design cycle number
    #file_save     # don’t delete old design cycle files

responses,
```

```
    id_responses = ‘R1’
    num_objective_functions = 1
    num_nonlinear_inequality_constraints = 1
    nonlinear_inequality_lower_bounds = 1.0e-8
    no_gradients
    no_hessians

responses,
    id_responses = ‘R2’
  num_objective_functions = 1
    num_nonlinear_inequality_constraints = 1
    nonlinear_inequality_lower_bounds = 1.0e-8
    #numerical_gradients
    #fd_gradient_step_size = .000001
    # to instead use analytic gradients returned by the simulator comment the
    # preceding two lines and uncomment the following:
    analytic_gradients
  no_hessians
```

VITA

Kristen Karman was born in Arlington, Texas to parents Debra and Steve Karman. She moved to Chattanooga with her family in 2003, where she attended and graduated from Notre Dame High School. After high school, she attended the University of Tennessee at Knoxville where she completed a bachelor's degree in Mathematics and Classical Languages, with a concentration in Latin language and a minor in Greek language. She accepted a graduate research assistantship with the SimCenter at the University of Tennessee at Chattanooga and completed her master's degree in Computational Engineering in December 2013. She will continue her studies at the University of Tennessee at Chattanooga to pursue a doctorate in Computational Engineering.